

1 **A SIMPLE AND EFFICIENT CONVEX OPTIMIZATION BASED**
2 **BOUND-PRESERVING HIGH ORDER ACCURATE LIMITER FOR**
3 **CAHN–HILLIARD–NAVIER–STOKES SYSTEM ***

4 CHEN LIU[†], BEATRICE RIVIERE[‡], JIE SHEN [§], AND XIANGXIONG ZHANG [†]

5 **Abstract.** For time-dependent PDEs, the numerical schemes can be rendered bound-preserving
6 without losing conservation and accuracy, by a post processing procedure of solving a constrained
7 minimization in each time step. Such a constrained optimization can be formulated as a nonsmooth
8 convex minimization, which can be efficiently solved by first order optimization methods, if using the
9 optimal algorithm parameters. By analyzing the asymptotic linear convergence rate of the generalized
10 Douglas–Rachford splitting method, optimal algorithm parameters can be approximately expressed
11 as a simple function of the number of out-of-bounds cells. We demonstrate the efficiency of this simple
12 choice of algorithm parameters by applying such a limiter to cell averages of a discontinuous Galerkin
13 scheme solving phase field equations for 3D demanding problems. Numerical tests on a sophisticated
14 3D Cahn–Hilliard–Navier–Stokes system indicate that the limiter is high order accurate, very efficient,
15 and well-suited for large-scale simulations. For each time step, it takes at most 20 iterations for the
16 Douglas–Rachford splitting to enforce bounds and conservation up to the round-off error, for which
17 the computational cost is at most $80N$ with N being the total number of cells.

18 **Key words.** Douglas–Rachford splitting, nearly optimal parameters, bound-preserving limiter,
19 discontinuous Galerkin method, Cahn–Hilliard–Navier–Stokes, high order accuracy

20 **MSC codes.** 65K10, 65M60, 65M12, 90C25

21 **1. Introduction.**

22 **1.1. Objective and motivation.** We are interested in a simple approach to
23 enforce bound-preserving property of a high order accurate scheme for phase field
24 models, without destroying conservation and accuracy. Many numerical methods,
25 especially high order accurate schemes, do not preserve bounds. For the sake of both
26 physical meaningfulness and robustness of numerical computation, it is critical to
27 enforce both conservation and bounds.

28 Bound-preserving schemes have been well studied in the literature for equations
29 like hyperbolic and parabolic PDEs. One popular approach of constructing a bound-
30 preserving high order scheme was introduced in [44, 45] for conservation laws, which
31 can be extended to parabolic equations [40, 39] and Navier–Stokes equations [12, 43],
32 as well as implicit or semi-implicit time discretizations [35, 31]. However, this method,
33 and most of other popular bound-preserving schemes for conservation laws and para-
34 bolic equations such as exponential time differencing [10], are based on the fact that
35 the simplest low order scheme is bound-preserving, which is no longer true for a fourth
36 order PDE like the Cahn–Hilliard equation, unless a very special implementation is
37 used such as implicit treatment of a logarithmic potential [6].

38 A simple cut-off without enforcing conservation does not destroy accuracy but
39 it is of little interest, because convergence might be lost due to loss of conservation.
40 A meaningful objective is to enforce bounds without destroying conservation. For
41 the Cahn–Hilliard equation, an exponential function transform approach was used in

*Submitted to the editors DATE.

Funding: X.Z. is supported by NSF DMS-2208518. J. S. is supported by NSFC 12371409.

[†]Department of Mathematics, Purdue University, 150 North University Street, West Lafayette, Indiana 47907 (liu3373@purdue.edu, zhan1966@purdue.edu).

[‡]Department of Computational Applied Mathematics and Operations Research, Rice University, 6100 Main Street, Houston, Texas 77005 (riviere@rice.edu).

[§] Eastern Institute of Technology, Ningbo, Zhejiang 315200, P.R. China (jshen@eitech.edu.cn).

[23], with conservation achieved up to some small time error. If the logarithmic energy potential is used and treated implicitly, bounds can also be ensured [6]. A Lagrange multiplier approach in [7, 8] provides a new interpretation for the cut-off method, and can preserve mass by solving a nonlinear algebraic equation for the additional space independent Lagrange multiplier. Even though the flux limiting [25, 42, 22, 11] can be formally extended to Cahn–Hilliard equation [17, 30], it is not clear whether flux limiters can preserve high order accuracy for a fourth order PDE. Recently a bound-preserving finite volume scheme, which is first order accurate in time and second order accurate in space, has been constructed for the Cahn–Hilliard equation [1].

In practice, the logarithmic potential causes additional difficulty in nonlinear system solvers in many schemes, thus the double well polynomial potential with a degenerate mobility is often used as an easier surrogate. With the double well potential, numerical schemes might violate the bounds much more since it does not enforce bounds $\phi \in [-1, 1]$ like the log potential. In this paper, we will explore a simple and efficient high order accurate post processing procedure for preserving bounds and conservation up to round-off errors, such that it can be easily applied to any numerical method solving the Cahn–Hilliard equation, especially for the polynomial potential.

1.2. A bound-preserving limiter via convex minimization. Consider a scalar PDE as an example. Assume its solution u satisfies $m \leq u \leq M$ for all time and location, where m and M are constant bounds. For simplicity, we only consider enforcing cell averages in a high order accurate discontinuous Galerkin (DG) scheme by the convex minimization, then using the simple Zhang–Shu limiter in [44, 45] to enforce bounds of point values of the DG solution. But this convex minimization approach can be easily extended to enforcing bounds of point values for any other numerical scheme such as finite difference and continuous finite element methods.

Let \bar{u}_i ($i = 1, \dots, N$) be all the DG solution cell averages at time step n on a uniform mesh. Given $\mathbf{u} = [\bar{u}_1 \ \bar{u}_2 \ \dots \ \bar{u}_N]^T \in \mathbb{R}^N$, we would like to post process it to $\mathbf{x} = [x_1 \ x_2 \ \dots \ x_N]^T \in \mathbb{R}^N$ such that it is bound preserving $x_i \in [m, M]$, conservative $\sum_i x_i = \sum_i \bar{u}_i$, and accurate in the sense that $\|\mathbf{x} - \mathbf{u}\|$ should be small. Namely, we consider minimize $\|\mathbf{x} - \mathbf{u}\|$ under constraints $x_i \in [m, M]$ and $\sum_{i=1}^N x_i = \sum_{i=1}^N \bar{u}_i$. To change as few cell averages as possible, the convex ℓ^1 -norm is often used to approximate the NP-hard ℓ^0 -norm. The ℓ^1 -norm is nonsmooth without any strong convexity, thus the minimization might still be too expensive to solve. For the sake of efficiency, we propose the ℓ^2 -norm instead:

$$(1.1) \quad \min_{\mathbf{x}} \|\mathbf{x} - \mathbf{u}\|_2^2 \quad \text{s.t.} \quad x_i \in [m, M] \quad \text{and} \quad \sum_{i=1}^N x_i = \sum_{i=1}^N \bar{u}_i.$$

Obviously, the minimizer to (1.1) is conservative and bound-preserving. The justification of accuracy is also straightforward, as long as \mathbf{u} is an accurate numerical solution, which is a reasonable assumption and has been proved to hold for many DG schemes of a variety of PDEs, e.g., see [29] for Cahn–Hilliard–Navier–Stokes (CHNS) equations. Let \bar{u}_i^* and \bar{u}_i^0 be the cell averages of the exact solution at time t^n and initial condition, respectively. Then $\sum_i \bar{u}_i^* = \sum_i \bar{u}_i^0 = \sum_i \bar{u}_i$ and $\bar{u}_i^* \in [m, M]$ imply that \mathbf{u}^* is a feasible point satisfying the constraints of (1.1). The minimizer \mathbf{x}^* to (1.1) then satisfies $\|\mathbf{x}^* - \mathbf{u}\|_2 \leq \|\mathbf{u}^* - \mathbf{u}\|_2$, thus $\|\mathbf{x}^* - \mathbf{u}^*\|_2 \leq \|\mathbf{x}^* - \mathbf{u}\|_2 + \|\mathbf{u} - \mathbf{u}^*\|_2 \leq 2\|\mathbf{u}^* - \mathbf{u}\|_2$. Therefore, the limiter (1.1) does not lose the order of accuracy.

86 **1.3. Efficient convex optimization algorithms.** The main catch of using
 87 (1.1) in a large scale computation, is the possible huge cost of solving (1.1) to machine
 88 accuracy, unless proven or shown otherwise, which is our main focus. It is a convention

89 use the indicator function $\iota_{\Omega}(\mathbf{x}) = \begin{cases} 0, & \mathbf{x} \in \Omega \\ +\infty, & \mathbf{x} \notin \Omega \end{cases}$ for any set Ω , to rewrite (1.1) as:

$$90 \quad (1.2) \quad \min_{\mathbf{x}} \frac{\alpha}{2} \|\mathbf{x} - \mathbf{u}\|_2^2 + \iota_{\Lambda_1}(\mathbf{x}) + \iota_{\Lambda_2}(\mathbf{x}),$$

91 where $\alpha > 0$ is a parameter and the sets Λ_1 and Λ_2 are $\Lambda_1 = \{\mathbf{x} : \sum_i x_i =$
 92 $\sum_i \bar{u}_i\}$, $\Lambda_2 = \{\mathbf{x} : x_i \in [m, M]\}$. The two indicator functions in (1.2) are convex
 93 but nonsmooth, and the ℓ^2 term is strongly convex, thus (1.2) has a unique minimizer
 94 \mathbf{x}^* . Many optimization algorithms, e.g., fast proximal gradient (FISTA) [34, 3] ap-
 95 plied to (1.2), can be proven to converge linearly. But a provable global linear rate is
 96 usually quite pessimistic, much slower than the actual convergence rate. It is possible
 97 to obtain sharp asymptotic rate for methods like the generalized Douglas–Rachford
 98 splitting solving ℓ^1 minimization [9], which can be used for designing best parameters.
 99 So we consider the generalized Douglas–Rachford splitting [26], which is equivalent
 100 to some other popular methods such as PDHG [5], ADMM [13], dual split Bregman
 101 [20], see also [9] and references therein for the equivalence.

102 **1.4. The generalized Douglas–Rachford splitting method.** Splitting al-
 103 gorithms naturally arise for composite optimization of the form

$$104 \quad (1.3a) \quad \min_{\mathbf{x}} f(\mathbf{x}) + g(\mathbf{x}),$$

where functions f and g are convex and have simple subdifferentials and resolvents.
 Let ∂f and ∂g denote the subdifferentials of f and g . Their resolvents are defined as

$$J_{\gamma\partial f} = (\mathbf{I} + \gamma\partial f)^{-1} = \operatorname{argmin}_{\mathbf{z}} \gamma f(\mathbf{z}) + \frac{1}{2} \|\mathbf{z} - \mathbf{x}\|_2^2, \quad \gamma > 0,$$

$$J_{\gamma\partial g} = (\mathbf{I} + \gamma\partial g)^{-1} = \operatorname{argmin}_{\mathbf{z}} \gamma g(\mathbf{z}) + \frac{1}{2} \|\mathbf{z} - \mathbf{x}\|_2^2, \quad \gamma > 0.$$

105 We rewrite (1.2) into $\min_{\mathbf{x}} f(\mathbf{x}) + g(\mathbf{x})$ by defining

$$106 \quad (1.3b) \quad f(\mathbf{x}) = \frac{\alpha}{2} \|\mathbf{x} - \mathbf{u}\|_2^2 + \iota_{\Lambda_1}(\mathbf{x}) \quad \text{and} \quad g(\mathbf{x}) = \iota_{\Lambda_2}(\mathbf{x}),$$

107 where two sets are $\Lambda_1 = \{\mathbf{x} : \mathbf{A}\mathbf{x} = b\}$ and $\Lambda_2 = \{\mathbf{x} : m \leq \mathbf{x} \leq M\}$, with
 108 $\mathbf{A} = [1 \ \cdots \ 1]$, $b = \sum_i \bar{u}_i$, and $m \leq \mathbf{x} \leq M$ denoting entrywise inequality. The
 109 subdifferentials and resolvents can be explicitly given as

$$110 \quad (1.4) \quad \partial f(\mathbf{x}) = \alpha(\mathbf{x} - \mathbf{u}) + \mathcal{R}(\mathbf{A}^T), \quad J_{\gamma\partial f}(\mathbf{x}) = \frac{1}{\gamma\alpha + 1} (\mathbf{A}^+(b - \mathbf{A}\mathbf{x}) + \mathbf{x}) + \frac{\gamma\alpha}{\gamma\alpha + 1} \mathbf{u},$$

111

$$112 \quad (1.5) \quad [\partial g(\mathbf{x})]_i = \begin{cases} [0, +\infty], & \text{if } x_i = M, \\ 0, & \text{if } x_i \in (m, M), \\ [-\infty, 0], & \text{if } x_i = m. \end{cases} \quad [J_{\gamma\partial g}(\mathbf{x})]_i = \min(\max(x_i, m), M),$$

113

114 where $\mathcal{R}(\mathbf{A}^T)$ denotes the range of the matrix \mathbf{A}^T and $\mathbf{A}^+ = \mathbf{A}^T(\mathbf{A}\mathbf{A}^T)^{-1}$.

115 Define reflection operators as $R_{\gamma\partial f} = 2J_{\gamma\partial f} - I$ and $R_{\gamma\partial g} = 2J_{\gamma\partial g} - I$, where I
 116 denotes the identity operator. The generalized Douglas–Rachford splitting for (1.3a)
 117 can be written as:

$$118 \quad (1.6) \quad \begin{cases} \mathbf{y}^{k+1} = \lambda \frac{R_{\gamma\partial f} R_{\gamma\partial g} + I}{2} \mathbf{y}^k + (1 - \lambda) \mathbf{y}^k = \lambda J_{\gamma\partial f} \circ (2J_{\gamma\partial g} - I) \mathbf{y}^k + (1 - \lambda J_{\gamma\partial g}) \mathbf{y}^k \\ \mathbf{x}^{k+1} = J_{\gamma\partial g}(\mathbf{y}^{k+1}) \end{cases}$$

119 where \mathbf{y} is an auxiliary variable, $\gamma > 0$ is step size, and $\lambda \in (0, 2)$ is a parameter.
 120 For two convex functions $f(\mathbf{x})$ and $g(\mathbf{x})$, (1.6) converges for any $\gamma > 0$ and any fixed
 121 $\lambda \in (0, 2)$, see [26]. If one function is strongly convex, then $\lambda = 2$ also converges.

122 1.5. The bound-preserving post processing procedure for DG schemes.

123 At time step n , let $u_i(x, y, z)$ be the DG polynomial on a uniform mesh in the i -th
 124 cell with cell average \bar{u}_i . We define the following bound-preserving limiter:

125 **Step I:** Solve (1.2) to post process the cell averages. Let $c = \frac{1}{\alpha\gamma+1}$, then the
 126 iteration (1.6) on (1.3) can be explicitly written as:

$$127 \quad (1.7a) \quad \begin{cases} \mathbf{x}^k & = \min(\max(\mathbf{y}^k, m), M) \\ \mathbf{z}^k & = 2\mathbf{x}^k - \mathbf{y}^k \\ \mathbf{y}^{k+1} & = \lambda c(\mathbf{z}^k - \mathbf{1}[\frac{1}{N}(\sum_i z_i^k - b)]) + \lambda(1 - c)\mathbf{u} + \mathbf{y}^k - \lambda\mathbf{x}^k \end{cases},$$

128 where $\mathbf{1}$ is the constant one vector of size N and $b = \sum_i \bar{u}_i$ is a constant, $\lambda \in (0, 2]$
 129 is the fixed relaxation parameter. Each iterate \mathbf{x}^k is bound-preserving but is not
 130 conservative until converging to the minimizer \mathbf{x}^* . We iterate (1.7a) until relative
 131 change is small enough $\|\mathbf{y}^{k+1} - \mathbf{y}^k\|_2 \leq \epsilon$, to get an approximated minimizer \mathbf{x}^* to
 132 (1.2), for which the conservation would be satisfied up to round-off errors. We then
 133 modify DG polynomials by modifying the cell averages, i.e., shift them by a constant:

$$134 \quad (1.7b) \quad \tilde{u}_i(x, y, z) = u_i(x, y, z) - \bar{u}_i + x_i^*, \quad i = 1, \dots, N.$$

135 **Step II:** Cell averages of modified DG polynomials $\tilde{u}_i(x, y, z)$ are in the range
 136 $[m, M]$, so we can apply the simple scaling limiter by Zhang and Shu in [44, 45] to
 137 further enforce bounds at quadrature points, without losing conservation and accu-
 138 racy. Let S_i be the set of interested points in each cell, then the Zhang–Shu limiter
 139 for the polynomial $\tilde{u}_i(x, y, z)$ with cell average $x_i^* \in [m, M]$ is given as

$$140 \quad (1.8) \quad \hat{u}_i(x, y, z) = \theta(\tilde{u}_i(x, y, z) - x_i^*) + x_i^*, \quad \theta = \min \left\{ 1, \frac{|m - x_i^*|}{|m_i - x_i^*|}, \frac{|M - x_i^*|}{|M_i - x_i^*|} \right\},$$

141 where $m_i = \min_{(x,y,z) \in S_i} \tilde{u}_i(x, y, z)$ and $M_i = \max_{(x,y,z) \in S_i} \tilde{u}_i(x, y, z)$. See the appendix in [43]
 142 for a rigorous proof of the high order accuracy of (1.8).

143 We emphasize that the Zhang–Shu limiter (1.8) can preserve bounds or positiv-
 144 ity provided that the cell averages are within bounds or are positive, which can be
 145 proven for DG methods coupled with the limiter (1.8) for hyperbolic problems in-
 146 cluding scalar conservation laws, compressible Euler and compressible Navier–Stokes
 147 equations [44, 45, 43], because DG methods with suitable numerical fluxes satisfy a
 148 weak monotonicity property for these problems [43]. However, such a weak mono-
 149 tonicity property is simply not true for high order DG schemes solving fourth order
 150 PDEs. Thus, if using only the limiter (1.8), the high order DG methods will not be
 151 bound-preserving for Cahn–Hilliard equations. For all the numerical tests shown in
 152 this paper, DG methods with only the Zhang–Shu limiter will produce cell averages
 153 outside of the range $[-1, 1]$.

154 **1.6. The main results.** We will analyze asymptotic convergence rate of iteration
 155 (1.7a) and give a sharp convergence rate formula, by which it is possible to pick
 156 up nearly optimal combination of parameters $c = \frac{1}{\alpha\gamma+1}$ and λ to achieve fast conver-
 157 gence for the iteration (1.7a). The asymptotic linear convergence rate we derive for
 158 (1.2) is similar to the one for ℓ^1 minimization in [9]. These rate formulae depend on
 159 the unknown \mathbf{x}^* , so usually it is impossible to use the formulae for tuning algorithm
 160 parameters, unless \mathbf{x}^* can be easily estimated. For (1.2), it is possible to pick up a
 161 nearly optimal combination of optimization algorithm parameters by only calculating
 162 number of bad cells $\bar{u}_i \notin [m, M]$, which is the first main result of this paper.

163 Let \hat{r} be the number of bad cells $\bar{u}_i \notin [m, M]$, and let $\hat{\theta} = \cos^{-1} \sqrt{\frac{\hat{r}}{N}}$, then our
 164 analysis suggests the following simple choice of nearly optimal parameters:

$$165 \quad (1.9) \quad \begin{cases} c = \frac{1}{2}, \lambda = \frac{4}{2 - \cos(2\hat{\theta})}, & \text{if } \hat{\theta} \in (\frac{3}{8}\pi, \frac{1}{2}\pi], \\ c = \frac{1}{(\cos \hat{\theta} + \sin \hat{\theta})^2}, \lambda = \frac{2}{1 + \frac{1}{1 + \cot \hat{\theta}} - \frac{1}{(\cos \hat{\theta} + \sin \hat{\theta})^2}}, & \text{if } \hat{\theta} \in (\frac{1}{4}\pi, \frac{3}{8}\pi], \\ c = \frac{1}{(\cos \hat{\theta} + \sin \hat{\theta})^2}, \lambda = 2, & \text{if } \hat{\theta} \in (0, \frac{1}{4}\pi]. \end{cases}$$

166 We emphasize that both c and λ should be the constants w.r.t. iteration index k in
 167 (1.7a), once they are chosen by (1.9). Notice that $\lambda(1-c)\mathbf{u}$ is a constant for the itera-
 168 tion (1.7a) and each entry of $\mathbf{z}^k - \mathbf{1}[\frac{1}{N}(\sum_i z_i^k - b)]$ can be computed by $z_i^k - [\frac{1}{N}(\sum_i z_i^k - b)]$,
 169 thus if only counting number of computing multiplications, min, and max, the compu-
 170 tational complexity of each iteration in (1.7a) is $4N$. By using the parameters (1.9),
 171 it takes at most 20 iterations of (1.7a) to converge in all our numerical tests, thus
 172 the cost of iterating (1.7a) until convergence would be at most $80N$, which is highly
 173 efficient and well-suited for large-scale simulations.

174 The numerical observation of at most 20 iterations can also be explained by the
 175 asymptotic convergence rate analysis, which is another main result. Assuming the
 176 number of bad cells $\bar{u}_i \notin [m, M]$ is much smaller than the number of total cells N , we
 177 will show that the asymptotic convergence rate of (1.7a) using (1.9) is given by

$$178 \quad (1.10) \quad -\frac{\cos(2\theta)}{2 - \cos(2\theta)} \approx -\frac{\cos(2\hat{\theta})}{2 - \cos(2\hat{\theta})} = \frac{1 - 2\cos \hat{\theta}^2}{3 - 2\cos \hat{\theta}^2} = \frac{1 - 2\frac{\hat{r}}{N}}{3 - 2\frac{\hat{r}}{N}} \approx \frac{1}{3}, \quad \text{if } \hat{r} \ll N,$$

179 with $\theta(\mathbf{x}^*)$ being an unknown angle, which can be approximated by $\hat{\theta}$. If the ratio of
 180 bad cells is very small, (1.7a) will have a local convergence rate almost like $\|\mathbf{y}^k - \mathbf{y}^*\| \leq$
 181 $C(\frac{1}{3})^k$, which would take around 30 iterations to reach around 1E-15 if $C = 1$.

182 **1.7. Organization of the paper.** The rest of the paper is organized as follows.
 183 In Section 2, we analyze the asymptotic linear convergence rate of the Douglas-
 184 Rachford splitting (1.6) and (1.7a), and derive the parameter guideline (1.9). In
 185 Section 3, we discuss an application of our bound-preserving limiting strategy to an
 186 important phase-field model, the CHNS system. The numerical tests are given in
 187 Section 4. Section 5 are concluding remarks.

188 **2. Asymptotic linear convergence rate analysis.** In this section, we de-
 189 rive the asymptotic linear convergence rate of generalized Douglas-Rachford splitting
 190 (1.6) for solving the minimization problem (1.3). The discussion in this section fol-
 191 lows closely the analysis for ℓ^1 minimization in [9]. Even though ℓ^1 minimization is
 192 harder than ℓ^2 minimization, the analysis for (1.3) is not necessarily a straightforward
 193 extension of those in [9] because (1.4) and (1.5) are different from operators in [9].

194 For convenience, let $F = \partial f$ and $G = \partial g$ denote the subdifferential operators. Let
 195 $\mathbf{S}(\mathbf{x})$ be the cut-off operator, i.e., $[\mathbf{J}_{\gamma G}(\mathbf{x})]_i = [\mathbf{S}(\mathbf{x})]_i = \min(\max(x_i, m), M)$.

196 We keep the discussion a bit more general by considering a general linear con-
 197 straint $\mathbf{A}\mathbf{x} = b = \mathbf{A}\mathbf{u}$ in the function $f(\mathbf{x})$ in (1.3b), and assume \mathbf{A} has less number of
 198 rows than the number of columns, with full row rank such that $\mathbf{A}^+ = \mathbf{A}^T(\mathbf{A}\mathbf{A}^T)^{-1}$ is
 199 well defined. When needed, we will plug in the special case $\mathbf{A} = \begin{bmatrix} 1 & 1 & \cdots & 1 \end{bmatrix}$.

200 **2.1. The fixed point set.** Let $\mathbf{P}(\mathbf{x}) = \mathbf{A}^+(b - \mathbf{A}\mathbf{x}) + \mathbf{x}$ denote the projection
 201 operator. Then, the resolvents can be written as $\mathbf{J}_{\gamma F}(\mathbf{x}) = \frac{1}{\gamma\alpha+1}\mathbf{P}(\mathbf{x}) + \frac{\gamma\alpha}{\gamma\alpha+1}\mathbf{u}$ and
 202 $\mathbf{J}_{\gamma G}(\mathbf{x}) = \mathbf{S}(\mathbf{x})$. Let \mathbf{T}_γ denote the iteration operator for \mathbf{y} in (1.6), then it becomes:

$$203 \quad (2.1) \quad \mathbf{T}_\gamma = \frac{\lambda}{\gamma\alpha+1}\mathbf{P} \circ (2\mathbf{S} - \mathbf{I}) + (\mathbf{I} - \lambda\mathbf{S}) + \frac{\lambda\gamma\alpha}{\gamma\alpha+1}\mathbf{u}.$$

204 The fixed point \mathbf{y}^* of \mathbf{T}_γ is not the minimizer of (1.3), while $\mathbf{x}^* = \mathbf{J}_{\gamma G}(\mathbf{y}^*) = \mathbf{S}(\mathbf{y}^*)$ is
 205 the minimizer. The fixed point set of the operator \mathbf{T}_γ has the following structure.

THEOREM 2.1. *The set of fixed point of operator \mathbf{T}_γ is*

$$\Pi = \{\mathbf{y}^* : \mathbf{y}^* = \mathbf{x}^* + \gamma\boldsymbol{\eta}, \boldsymbol{\eta} \in -\partial f(\mathbf{x}^*) \cap \partial g(\mathbf{x}^*)\}.$$

206 *Proof.* We first show any $\mathbf{y}^* \in \Pi$ is a fixed point of the operator \mathbf{T}_γ . $\forall \boldsymbol{\eta} \in \partial g(\mathbf{x}^*)$
 207 in (1.5), we have $\mathbf{S}(\mathbf{y}^*) = \mathbf{x}^*$, since the i -th entry of the vector $\mathbf{y}^* = \mathbf{x}^* + \gamma\boldsymbol{\eta}$ satisfies

$$208 \quad [\mathbf{y}^*]_i \begin{cases} \in [M, +\infty], & \text{if } x_i^* = M, \\ = x_i^*, & \text{if } x_i^* \in (m, M), \\ \in [-\infty, m], & \text{if } x_i^* = m. \end{cases}$$

209 Thus, we have $\mathbf{P} \circ (2\mathbf{S} - \mathbf{I})\mathbf{y}^* = \mathbf{P}(2\mathbf{x}^* - \mathbf{y}^*) = \mathbf{P}(\mathbf{x}^* - \gamma\boldsymbol{\eta}) = \mathbf{x}^* - \gamma\boldsymbol{\eta} + \gamma\mathbf{A}^+\mathbf{A}\boldsymbol{\eta}$, where
 210 $\mathbf{A}\mathbf{x}^* = b$ is used. And $\boldsymbol{\eta} \in -\partial f(\mathbf{x}^*)$ in (1.4) implies that there exists $\boldsymbol{\xi}$ such that
 211 $\boldsymbol{\eta} = -\alpha(\mathbf{x}^* - \mathbf{u}) + \mathbf{A}^T\boldsymbol{\xi}$. Multiplying both sides by \mathbf{A} , with $\mathbf{A}\mathbf{x}^* = b = \mathbf{A}\mathbf{u}$ we get
 212 $\mathbf{A}\boldsymbol{\eta} = \mathbf{A}\mathbf{A}^T\boldsymbol{\xi}$, thus $\boldsymbol{\xi} = (\mathbf{A}\mathbf{A}^T)^{-1}\mathbf{A}\boldsymbol{\eta}$ and $\gamma\boldsymbol{\eta} = -\gamma\alpha(\mathbf{x}^* - \mathbf{u}) + \gamma\mathbf{A}^+\mathbf{A}\boldsymbol{\eta}$. Then, we have
 213 $\mathbf{P} \circ (2\mathbf{S} - \mathbf{I})\mathbf{y}^* = (\gamma\alpha + 1)\mathbf{x}^* - \gamma\alpha\mathbf{u}$. Therefore

$$214 \quad \mathbf{T}_\gamma(\mathbf{y}^*) = \frac{\lambda}{\gamma\alpha+1}((\gamma\alpha+1)\mathbf{x}^* - \gamma\alpha\mathbf{u}) + \mathbf{y}^* - \lambda\mathbf{x}^* + \frac{\lambda\gamma\alpha}{\gamma\alpha+1}\mathbf{u} = \mathbf{y}^*.$$

215 Next, we show any fixed point \mathbf{y}^* belongs to set Π . Let $\boldsymbol{\eta} = (\mathbf{y}^* - \mathbf{x}^*)/\gamma$. Then, \mathbf{y}^*
 216 being a fixed point implies $\mathbf{J}_{\gamma G}(\mathbf{y}^*) = \mathbf{x}^*$. Recall that $\mathbf{J}_{\gamma G} = \mathbf{S}$, we have

- 217 i. if $x_i^* + \gamma\eta_i \geq M$, then $x_i^* = \mathbf{S}(x_i^* + \gamma\eta_i) = M$, thus $\eta_i \in [0, +\infty]$;
- 218 ii. if $x_i^* + \gamma\eta_i \in (m, M)$, then $x_i^* = \mathbf{S}(x_i^* + \gamma\eta_i) = x_i^* + \gamma\eta_i$, thus $\eta_i = 0$;
- 219 iii. if $x_i^* + \gamma\eta_i \leq m$, then $x_i^* = \mathbf{S}(x_i^* + \gamma\eta_i) = m$, thus $\eta_i \in [-\infty, 0]$.

220 So $\boldsymbol{\eta} \in \partial g(\mathbf{x}^*)$. And $\mathbf{y}^* = \mathbf{T}_\gamma(\mathbf{y}^*)$ is equivalent to $\mathbf{y}^* = \frac{1}{2}(\mathbf{R}_{\gamma F}\mathbf{R}_{\gamma G} + \mathbf{I})\mathbf{y}^* + (1 - \lambda)\mathbf{y}^*$,
 221 which implies $\mathbf{y}^* = \mathbf{R}_{\gamma F}\mathbf{R}_{\gamma G}(\mathbf{y}^*)$. Recall $\mathbf{J}_{\gamma G}(\mathbf{y}^*) = \mathbf{x}^*$ and $\mathbf{y}^* = \mathbf{x}^* + \gamma\boldsymbol{\eta}$, we have

$$222 \quad \mathbf{y}^* = \mathbf{R}_{\gamma F}(2\mathbf{J}_{\gamma G}(\mathbf{y}^*) - \mathbf{y}^*) = \mathbf{R}_{\gamma F}(\mathbf{x}^* - \gamma\boldsymbol{\eta}) = 2\mathbf{J}_{\gamma F}(\mathbf{x}^* - \gamma\boldsymbol{\eta}) - (\mathbf{x}^* - \gamma\boldsymbol{\eta}).$$

223 So $\mathbf{x}^* = \mathbf{J}_{\gamma F}(\mathbf{x}^* - \gamma\boldsymbol{\eta})$, which implies $\mathbf{x}^* = \operatorname{argmin}_z \gamma f(z) + \frac{1}{2}\|z - (\mathbf{x}^* - \gamma\boldsymbol{\eta})\|_2^2$. By the
 224 critical point equation, we have $\mathbf{0} \in \gamma\partial f(\mathbf{x}^*) + \gamma\boldsymbol{\eta}$ thus $\boldsymbol{\eta} \in -\partial f(\mathbf{x}^*)$. \square

225 Let $\mathcal{B}_r(\mathbf{z})$ denote a closed ball in ℓ^2 -norm centered at \mathbf{z} with radius r . Define set \mathcal{Q} :

$$226 \quad \mathcal{Q} = Q_1 \otimes Q_2 \otimes \cdots \otimes Q_n, \quad \text{where } Q_i = \begin{cases} [M, +\infty], & \text{if } x_i^* = M, \\ (m, M), & \text{if } x_i^* \in (m, M), \\ [-\infty, m], & \text{if } x_i^* = m. \end{cases}$$

227 For any fixed point \mathbf{y}^* , the Theorem 2.1 implies there exists an $\boldsymbol{\eta} = \frac{1}{\gamma}(\mathbf{y}^* - \mathbf{x}^*) \in \partial g(\mathbf{x}^*)$
 228 and by (1.5) we have $\mathbf{x}^* + \gamma\boldsymbol{\eta} \in \mathcal{Q}$ for any $\gamma > 0$, which gives $\mathbf{y}^* \in \mathcal{Q}$. Let $\epsilon \geq 0$ be the
 229 least upper bound such that $\mathcal{B}_\epsilon(\mathbf{y}^*) \subset \mathcal{Q}$. If $\epsilon > 0$, then \mathbf{y}^* is an interior fixed point
 230 and we call this the standard case; otherwise, \mathbf{y}^* is a boundary fixed point and we
 231 call this the non-standard case. In the standard case that the sequence \mathbf{y}^k converges
 232 to an interior fixed point \mathbf{y}^* . There exists a large enough integer $K > 0$ such that
 233 $\|\mathbf{y}^K - \mathbf{y}^*\|_2 < \epsilon$ holds. For any $k \geq K$, the operator T_γ is nonexpansive [26], so

$$234 \quad \|\mathbf{y}^k - \mathbf{y}^*\|_2 = \|T_\gamma(\mathbf{y}^{k-1}) - T_\gamma(\mathbf{y}^*)\|_2 \leq \|\mathbf{y}^{k-1} - \mathbf{y}^*\|_2 \leq \cdots \leq \|\mathbf{y}^K - \mathbf{y}^*\|_2 < \epsilon.$$

235 Thus, after taking the generalized Douglas–Rachford iteration (1.6) sufficiently many
 236 times, the iterates will always belong to the ball $\mathcal{B}_\epsilon(\mathbf{y}^*) \subset \mathcal{Q}$, namely the iteration
 237 enters the asymptotic convergence regime and the cut-off location does not change.

238 In the rest of this paper, we only focus on the standard case. The non-standard
 239 case can be analyzed by utilizing the same technique as in [9]. The non-standard case
 240 has not been observed in our numerical experiments.

241 **2.2. The characterization of the operator T_γ .** Assume the unique solution
 242 \mathbf{x}^* of the minimization problem (1.3) has r components equal to m or M . We further
 243 assume $r < N$, e.g., not all the cell averages will touch the boundary m or M , which
 244 is a quite reasonable assumption. We emphasize that r is unknown, unless \mathbf{x}^* is given.

245 Let \mathbf{e}_i ($i = 1, \dots, N$) be the standard basis of \mathbb{R}^N . Let \mathbf{e}_j ($j = i_1, \dots, i_r$) de-
 246 note the basis vectors corresponding to entries \mathbf{x}^* of being m or M . Let \mathbf{B} be the
 247 corresponding $r \times N$ selector matrix, i.e., $\mathbf{B} = [\mathbf{e}_{i_1}, \dots, \mathbf{e}_{i_r}]^\top$.

248 Recall that we only discuss the standard case, i.e., \mathbf{y}^* is in the interior of \mathcal{Q} .
 249 Then, in the asymptotic convergence regime, i.e., after sufficiently many iterations,
 250 the iterate \mathbf{y}_k will stay in the interior of \mathcal{Q} , thus the operator S has an expression

$$251 \quad (2.2) \quad S(\mathbf{y}) = \mathbf{y} - \mathbf{B}^+ \mathbf{B} \mathbf{y} + \sum_{j \in \{i_1, \dots, i_r\}} x_j^* \mathbf{e}_j.$$

252 Note, the j -th component of \mathbf{x}^* , namely the x_j^* in (2.2), takes value m or M for any
 253 $j \in \{i_1, \dots, i_r\}$. Let \mathbf{I}_N denote an $N \times N$ identity matrix.

254 **LEMMA 2.2.** *For any \mathbf{y} in the interior of \mathcal{Q} , and a standard fixed point \mathbf{y}^* in the*
 255 *interior of \mathcal{Q} , we have $T_\gamma(\mathbf{y}) - T_\gamma(\mathbf{y}^*) = \mathbf{T}_{c,\lambda}(\mathbf{y} - \mathbf{y}^*)$, where the matrix $\mathbf{T}_{c,\lambda}$ is given*
 256 *by*

$$257 \quad \mathbf{T}_{c,\lambda} = \lambda \left(c(\mathbf{I}_N - \mathbf{A}^+ \mathbf{A})(\mathbf{I}_N - \mathbf{B}^+ \mathbf{B}) + c\mathbf{A}^+ \mathbf{A} \mathbf{B}^+ \mathbf{B} + (1 - c)\mathbf{B}^+ \mathbf{B} \right) + (1 - \lambda)\mathbf{I}_N.$$

258 Here, $c = \frac{1}{\gamma\alpha+1}$ is a constant in $(0, 1)$.

Proof. By (2.2), $S(\mathbf{y}) - S(\mathbf{y}^*) = (\mathbf{I}_N - \mathbf{B}^+\mathbf{B})(\mathbf{y} - \mathbf{y}^*)$. So by (2.1),

$$\begin{aligned} T_\gamma(\mathbf{y}) - T_\gamma(\mathbf{y}^*) &= \frac{\lambda}{\gamma\alpha + 1} \left(P(2S(\mathbf{y}) - \mathbf{y}) - P(2S(\mathbf{y}^*) - \mathbf{y}^*) \right) + (\mathbf{y} - \mathbf{y}^*) - \lambda(S(\mathbf{y}) - S(\mathbf{y}^*)) \\ &= \frac{\lambda}{\gamma\alpha + 1} (\mathbf{I}_N - \mathbf{A}^+\mathbf{A})(\mathbf{I}_N - 2\mathbf{B}^+\mathbf{B})(\mathbf{y} - \mathbf{y}^*) + (\mathbf{y} - \mathbf{y}^*) - \lambda(\mathbf{I}_N - \mathbf{B}^+\mathbf{B})(\mathbf{y} - \mathbf{y}^*) \\ &= \frac{\lambda}{\gamma\alpha + 1} (\mathbf{I}_N - \mathbf{A}^+\mathbf{A})(\mathbf{I}_N - \mathbf{B}^+\mathbf{B})(\mathbf{y} - \mathbf{y}^*) + \frac{\lambda}{\gamma\alpha + 1} \mathbf{A}^+\mathbf{A}\mathbf{B}^+\mathbf{B}(\mathbf{y} - \mathbf{y}^*) \\ &\quad + \frac{\lambda\gamma\alpha}{\gamma\alpha + 1} \mathbf{B}^+\mathbf{B}(\mathbf{y} - \mathbf{y}^*) + (1 - \lambda)(\mathbf{y} - \mathbf{y}^*). \end{aligned}$$

Therefore, the matrix $\mathbf{T}_{c,\lambda}$ can be expressed as follows: □

$$\mathbf{T}_{c,\lambda} = \frac{\lambda}{\gamma\alpha + 1} \left((\mathbf{I}_N - \mathbf{A}^+\mathbf{A})(\mathbf{I}_N - \mathbf{B}^+\mathbf{B}) + \mathbf{A}^+\mathbf{A}\mathbf{B}^+\mathbf{B} \right) + \frac{\lambda\gamma\alpha}{\gamma\alpha + 1} \mathbf{B}^+\mathbf{B} + (1 - \lambda)\mathbf{I}_N.$$

DEFINITION 2.3. Let \mathcal{U} and \mathcal{V} be two subspaces of \mathbb{R}^N with $\dim(\mathcal{U}) = p \leq \dim(\mathcal{V})$. The principal angles $\theta_k \in [0, \frac{\pi}{2}]$ ($k = 1, \dots, p$) between \mathcal{U} and \mathcal{V} are recursively defined by

$$\cos \theta_k = \mathbf{u}_k^T \mathbf{v}_k = \max_{\mathbf{u} \in \mathcal{U}} \max_{\mathbf{v} \in \mathcal{V}} \mathbf{u}^T \mathbf{v},$$

$$\text{such that } \|\mathbf{u}\|_2 = \|\mathbf{v}\|_2 = 1, \mathbf{u}_j^T \mathbf{u} = 0, \mathbf{v}_j^T \mathbf{v} = 0, j = 1, 2, \dots, k-1.$$

The vectors $(\mathbf{u}_1, \dots, \mathbf{u}_p)$ and $(\mathbf{v}_1, \dots, \mathbf{v}_p)$ are principal vectors.

Our next goal is to decompose the matrix $\mathbf{T}_{c,\lambda}$ with principal angles between subspaces $\mathcal{N}(\mathbf{A})$ and $\mathcal{N}(\mathbf{B})$. To simplify the writeup, we define matrix $\mathbf{T} = (\mathbf{I}_N - \mathbf{A}^+\mathbf{A})(\mathbf{I}_N - \mathbf{B}^+\mathbf{B}) + \mathbf{A}^+\mathbf{A}\mathbf{B}^+\mathbf{B}$. Thus, we rewrite $\mathbf{T}_{c,\lambda} = \lambda(c\mathbf{T} + (1 - c)\mathbf{B}^+\mathbf{B}) + (1 - \lambda)\mathbf{I}_N$. Let \mathbf{A}_0 be an $N \times (N - 1)$ matrix whose columns are orthogonal basis of $\mathcal{N}(\mathbf{A})$ and \mathbf{A}_1 be an $N \times 1$ matrix whose columns are orthogonal basis of $\mathcal{R}(\mathbf{A}^T)$. Similarly, let \mathbf{B}_0 be an $N \times (N - r)$ matrix whose columns are orthogonal basis of $\mathcal{N}(\mathbf{B})$ and \mathbf{B}_1 be an $N \times r$ matrix whose columns are orthogonal basis of $\mathcal{R}(\mathbf{B}^T)$.

Since both $\mathbf{A}^+\mathbf{A}$ and $\mathbf{A}_1\mathbf{A}_1^T$ represent the projection to $\mathcal{R}(\mathbf{A}^T)$, we have $\mathbf{A}^+\mathbf{A} = \mathbf{A}_1\mathbf{A}_1^T$. Similarly, $\mathbf{I}_N - \mathbf{A}^+\mathbf{A} = \mathbf{A}_0\mathbf{A}_0^T$. Thus we have $\mathbf{T} = \mathbf{A}_0\mathbf{A}_0^T\mathbf{B}_0\mathbf{B}_0^T + \mathbf{A}_1\mathbf{A}_1^T\mathbf{B}_1\mathbf{B}_1^T$.

Define matrix $\mathbf{E}_0 = \mathbf{A}_0^T\mathbf{B}_0$ and matrix $\mathbf{E}_1 = \mathbf{A}_1^T\mathbf{B}_0$. Since $\mathbf{A}_0\mathbf{A}_0^T + \mathbf{A}_1\mathbf{A}_1^T = \mathbf{I}_N$, we have $\mathbf{B}_0 = (\mathbf{A}_0\mathbf{A}_0^T + \mathbf{A}_1\mathbf{A}_1^T)\mathbf{B}_0 = \mathbf{A}_0\mathbf{E}_0 + \mathbf{A}_1\mathbf{E}_1$. Therefore, we rewrite

$$\mathbf{B}_0\mathbf{B}_0^T = (\mathbf{A}_0\mathbf{E}_0 + \mathbf{A}_1\mathbf{E}_1)(\mathbf{E}_0^T\mathbf{A}_0^T + \mathbf{E}_1^T\mathbf{A}_1^T) = \begin{bmatrix} \mathbf{A}_0 & \mathbf{A}_1 \end{bmatrix} \begin{bmatrix} \mathbf{E}_0\mathbf{E}_0^T & \mathbf{E}_0\mathbf{E}_1^T \\ \mathbf{E}_1\mathbf{E}_0^T & \mathbf{E}_1\mathbf{E}_1^T \end{bmatrix} \begin{bmatrix} \mathbf{A}_0^T \\ \mathbf{A}_1^T \end{bmatrix}.$$

The singular value decomposition (SVD) of the $(N - 1) \times (N - r)$ matrix \mathbf{E}_0 is $\mathbf{E}_0 = \mathbf{U}_0 \cos \Theta \mathbf{V}^T$ with singular values $\cos \theta_1, \dots, \cos \theta_{N-r}$ in nonincreasing order. We know that θ_i ($i = 1, \dots, N - r$) are the principal angles between $\mathcal{N}(\mathbf{A})$ and $\mathcal{N}(\mathbf{B})$.

Notice $\mathbf{E}_1^T\mathbf{E}_1 = \mathbf{B}_0^T\mathbf{A}_1\mathbf{A}_1^T\mathbf{B}_0$ and $\mathbf{A}_1\mathbf{A}_1^T = \mathbf{I}_N - \mathbf{A}_0\mathbf{A}_0^T$, we have $\mathbf{E}_1^T\mathbf{E}_1 = \mathbf{B}_0^T\mathbf{B}_0 - \mathbf{B}_0^T\mathbf{A}_0\mathbf{A}_0^T\mathbf{B}_0 = \mathbf{I}_{N-r} - \mathbf{E}_0^T\mathbf{E}_0$. Recall the SVD of \mathbf{E}_0 , we have $\mathbf{E}_1^T\mathbf{E}_1 = \mathbf{V} \sin^2 \Theta \mathbf{V}^T$. Thus \mathbf{E}_1 can be expressed as $\mathbf{U}_1 \sin \Theta \mathbf{V}^T$, which is however not the SVD of \mathbf{E}_1 . To this end, let matrix $\tilde{\mathbf{A}} = [\mathbf{A}_0\mathbf{U}_0 \ \mathbf{A}_1\mathbf{U}_1]$, then (2.3) becomes

$$\mathbf{B}_0\mathbf{B}_0^T = \tilde{\mathbf{A}} \begin{bmatrix} \cos^2 \Theta & \sin \Theta \cos \Theta \\ \sin \Theta \cos \Theta & \sin^2 \Theta \end{bmatrix} \tilde{\mathbf{A}}^T.$$

295 Because of $\mathbf{B}_1 \mathbf{B}_1^T = \mathbf{I}_N - \mathbf{B}_0 \mathbf{B}_0^T$ and $\widetilde{\mathbf{A}} \widetilde{\mathbf{A}}^T = \mathbf{I}_N$, we have the decomposition

$$296 \quad (2.5) \quad \mathbf{B}_1 \mathbf{B}_1^T = \widetilde{\mathbf{A}} \begin{bmatrix} \sin^2 \Theta & -\sin \Theta \cos \Theta \\ -\sin \Theta \cos \Theta & \cos^2 \Theta \end{bmatrix} \widetilde{\mathbf{A}}^T.$$

297 Notice $\mathbf{A}_0 \mathbf{A}_0^T \widetilde{\mathbf{A}} = [\mathbf{A}_0 \mathbf{U}_0 \ \mathbf{O}_{N \times (N-r)}]$ and $\mathbf{A}_1 \mathbf{A}_1^T \widetilde{\mathbf{A}} = [\mathbf{O}_{N \times (N-r)} \ \mathbf{A}_1 \mathbf{U}_1]$, by (2.4) and
298 (2.5), we obtain

$$299 \quad (2.6) \quad \mathbf{T} = \widetilde{\mathbf{A}} \begin{bmatrix} \cos^2 \Theta & \sin \Theta \cos \Theta \\ -\sin \Theta \cos \Theta & \cos^2 \Theta \end{bmatrix} \widetilde{\mathbf{A}}^T.$$

300 Therefore, use (2.6) and consider $\mathbf{B}^+ \mathbf{B} = \mathbf{B}_1 \mathbf{B}_1^T$, the matrix $\mathbf{T}_{c,\lambda}$ becomes

$$301 \quad (2.7) \quad \mathbf{T}_{c,\lambda} = \widetilde{\mathbf{A}} \begin{bmatrix} \lambda c \cos^2 \Theta + \lambda(1-c) \sin^2 \Theta + (1-\lambda) \mathbf{I}_{N-r} & \lambda(2c-1) \sin \Theta \cos \Theta \\ -\lambda \sin \Theta \cos \Theta & \lambda \cos^2 \Theta + (1-\lambda) \mathbf{I}_{N-r} \end{bmatrix} \widetilde{\mathbf{A}}^T.$$

302 **2.3. Asymptotic convergence rate.** With the assumption $r < N$, there exists
303 a nonzero principal angle between subspaces $\mathcal{N}(\mathbf{A})$ and $\mathcal{N}(\mathbf{B})$. The following lemma
304 gives values of all the principal angles.

305 LEMMA 2.4. *The principal angles θ_i , $i = 1, \dots, N-r$, between subspaces $\mathcal{N}(\mathbf{A})$
306 and $\mathcal{N}(\mathbf{B})$ satisfy*

$$307 \quad (2.8) \quad \cos \theta_1 = \dots = \cos \theta_{N-r-1} = 1 \quad \text{and} \quad \cos \theta_{N-r} = \sqrt{\frac{r}{N}}.$$

308 *Proof.* Let $\mathcal{N}(\mathbf{A})^\perp$ denote the orthogonal complement of space $\mathcal{N}(\mathbf{A})$. Since $\mathbf{A} =$
309 $[1 \ 1 \ \dots \ 1] \in \mathbb{R}^{1 \times N}$, we have $\mathcal{N}(\mathbf{A})^\perp = \text{span}\{\mathbf{1}\}$. Recall the columns of \mathbf{B}_0 are
310 the orthogonal basis of $\mathcal{N}(\mathbf{B})$. The principal angles between $\mathcal{N}(\mathbf{A})^\perp$ and $\mathcal{N}(\mathbf{B})$ can be
311 computed via the SVD of $\frac{1}{\sqrt{N}} \mathbf{1}^T \mathbf{B}_0$. Each column of \mathbf{B}_0 is a standard basis e_j , where
312 $j \neq i_1, \dots, i_r$. Thus

$$313 \quad \left(\frac{1}{\sqrt{N}} \mathbf{1}^T \mathbf{B}_0 \right)^T \left(\frac{1}{\sqrt{N}} \mathbf{1}^T \mathbf{B}_0 \right) = \frac{1}{N} \begin{bmatrix} 1 & 1 & \dots & 1 \\ 1 & 1 & \dots & 1 \\ \vdots & \vdots & \ddots & \vdots \\ 1 & 1 & \dots & 1 \end{bmatrix}_{(N-r) \times (N-r)}.$$

314 The eigenvalues of the $(N-r) \times (N-r)$ matrix consisting of all ones, are $N-r$ and
315 $0, \dots, 0$. So the singular values of $\frac{1}{\sqrt{N}} \mathbf{1}^T \mathbf{B}_0$ are $\sqrt{\frac{N-r}{N}}$ and $0, \dots, 0$. We conclude
316 $\cos \theta_{N-r} = \sqrt{\frac{r}{N}}$, since the non-trivial principal angles between $\mathcal{N}(\mathbf{A})$ and $\mathcal{N}(\mathbf{B})$ and
317 the corresponding non-trivial principal angles between $\mathcal{N}(\mathbf{A})^\perp$ and $\mathcal{N}(\mathbf{B})$ sum up to
318 $\frac{\pi}{2}$, see the Theorem 2.7 in [24]. In addition, since the dimension of $\mathcal{N}(\mathbf{A})$ is $N-1$
319 and the dimension of $\mathcal{N}(\mathbf{B})$ is $N-r$, then as long as $N-r > 1$, from the definition of
320 principal angles, it is straightforward to see $\cos \theta_1 = \dots = \cos \theta_{N-r-1} = 1$. \square

321 By Lemma 2.4, there exists only one nonzero principal angle θ_{N-r} . By eliminating
322 zero columns in (2.7), (2.7) can be simplified as

$$323 \quad \mathbf{T}_{c,\lambda} = [\mathbf{A}_0 \mathbf{U}_0 \ \mathbf{A}_1] \begin{bmatrix} \mathbf{O}_{r-1} & & & \\ & (1-\lambda + \lambda c) \mathbf{I}_{N-r-1} & & \\ & & \lambda c \cos^2 \theta_{N-r} + \lambda(1-c) \sin^2 \theta_{N-r} + (1-\lambda) & \lambda(2c-1) \sin \theta_{N-r} \cos \theta_{N-r} \\ & & -\lambda \sin \theta_{N-r} \cos \theta_{N-r} & \lambda \cos^2 \theta_{N-r} + (1-\lambda) \end{bmatrix} \begin{bmatrix} \mathbf{U}_0^T \mathbf{A}_0^T \\ \mathbf{A}_1^T \end{bmatrix}.$$

324

325 From (2.7) we know the matrix $\mathbf{T}_{c,\lambda}$ is a nonnormal matrix, thus $\|\mathbf{T}_{c,\lambda}^k\|_2$ is sig-
 326 nificantly smaller than $\|\mathbf{T}_{c,\lambda}\|_2^k$ for sufficiently large k . Therefore, the asymptotic
 327 convergence rate is governed by $\lim_{k \rightarrow \infty} \|\mathbf{T}_{c,\lambda}^k\|_2^{\frac{1}{k}}$, which is equal to the norm of the
 328 eigenvalue of $\mathbf{T}_{c,\lambda}$ with the largest magnitude. We have

$$329 \det(\mathbf{T}_{c,\lambda} - \rho \mathbf{I}) = (\rho - 1 + \lambda - \lambda c)^{N-r-1} (\rho - 1 + \lambda c)^{r-1} \\
 330 \times [\rho^2 - (\lambda(c \cos 2\theta_{N-r} - 1) + 2)\rho + \lambda^2 c \sin^2 \theta_{N-r} + \lambda(c \cos 2\theta_{N-r} - 1) + 1].$$

333 By Lemma 2.4, the matrix $\mathbf{T}_{c,\lambda}$ has eigenvalues $\rho_0 = 1 - \lambda c$ and $\rho_1 = 1 - \lambda(1 - c)$
 334 corresponding to the principle angles $\theta_1, \dots, \theta_{N-r-1}$, Corresponding to the principle
 335 angle θ_{N-r} , the matrix $\mathbf{T}_{c,\lambda}$ has another two eigenvalues, ρ_2 and ρ_3 , satisfying the
 336 following quadratic equation:

$$337 (2.9) \quad \rho^2 - (\lambda(c \cos 2\theta_{N-r} - 1) + 2)\rho + \lambda^2 c \sin^2 \theta_{N-r} + \lambda(c \cos 2\theta_{N-r} - 1) + 1 = 0.$$

338 The discriminant of above equation is $\Delta = \lambda^2(c^2 \cos^2 2\theta_{N-r} - 2c + 1)$. The two solutions
 339 of $\Delta = 0$ are $[1 \pm \sin(2\theta_{N-r})]/\cos^2(2\theta_{N-r})$. Notice that $[1 + \sin(2\theta)]/\cos^2(2\theta) \geq 1$
 340 for any $\theta \in [0, \frac{\pi}{2}]$ and $c \in (0, 1)$. Let $c^* = [1 - \sin(2\theta_{N-r})]/\cos^2(2\theta_{N-r})$, then the
 341 magnitudes of ρ_2 and ρ_3 are:

$$342 \quad \text{if } c \leq c^*, \quad \text{then } |\rho_2| = \frac{1}{2} |\lambda c \cos(2\theta_{N-r}) - \lambda + 2 + \lambda \sqrt{\cos^2(2\theta_{N-r})c^2 - 2c + 1}|,$$

$$343 \quad |\rho_3| = \frac{1}{2} |\lambda c \cos(2\theta_{N-r}) - \lambda + 2 - \lambda \sqrt{\cos^2(2\theta_{N-r})c^2 - 2c + 1}|,$$

$$344 \quad \text{if } c > c^*, \quad \text{then } |\rho_2| = |\rho_3| = \sqrt{c\lambda^2 \sin^2 \theta_{N-r} - (1 - c \cos(2\theta_{N-r}))\lambda + 1}.$$

346 Recall the generalized Douglas–Rachford splitting (1.6) and (1.7a) converges due to
 347 convexity [26]. When the iterations enter the asymptotic regime (after the cut-off
 348 location of the operator S does not change), the convergence rate is governed by the
 349 largest magnitude of eigenvalues ρ_0, ρ_1, ρ_2 , and ρ_3 :

350 **THEOREM 2.5.** *For a standard fixed point of generalized Douglas–Rachford split-*
 351 *ting iteration as defined in Section 2.1, the asymptotic convergence rate of (1.6) solv-*
 352 *ing (1.3) is linear. There exists a sufficiently large $K > 0$, such that for any integer*
 353 *$k \geq K$, we have*

$$354 \quad \|\mathbf{y}^k - \mathbf{y}^*\|_2 \leq \tilde{C} \left(\min_{c,\lambda} \max\{|\rho_0|, |\rho_1|, |\rho_2|, |\rho_3|\} \right)^k,$$

355 where K and \tilde{C} may depend on \mathbf{A} , b , and \mathbf{y}^0 .

356 **2.4. A simple strategy of choosing nearly optimal parameters.** For solv-
 357 ing problem (1.3), after the iteration of algorithm (1.6) enters the asymptotic linear
 358 convergence regime, the rate of convergence is governed by the largest magnitude of
 359 ρ_0, ρ_1, ρ_2 , and ρ_3 . For seeking optimal parameters, we can safely ignore ρ_0 because it
 360 is straightforward to verify that $\rho_0 \leq \rho_1$ with the optimal parameters derived below.
 361 It is highly preferred to construct a guideline for selecting parameters c and λ such
 362 that for $\max\{|\rho_1|, |\rho_2|, |\rho_3|\}$ is reasonably small.

363 We first consider the case $\theta_{N-r} \in (\frac{\pi}{4}, \frac{\pi}{2}]$. It is easy to check $c^* = \frac{1}{(\cos \theta_{N-r} + \sin \theta_{N-r})^2} \in$
 364 $(\frac{1}{2}, 1]$. Define surfaces $\Gamma_i = \{(c, \lambda, z) : 0 < c < c^*, 0 < \lambda \leq 2, z = |\rho_i|\}$, where

365 $i \in \{1, 2, 3\}$. For any point $(c, \lambda, z) \in \Gamma_2 \cap \Gamma_3$, due to the fact that $|a + b| = |a - b|$
 366 implies $ab = 0$ for any $a, b \in \mathbb{R}$, we have $(\lambda c \cos(2\theta_{N-r}) - \lambda + 2)\sqrt{\Delta} = 0$. When $c < c^*$
 367 the discriminant $\Delta > 0$, we get $\lambda c \cos(2\theta_{N-r}) - \lambda + 2 = 0$. Thus, if there exists a point
 368 belongs to $\Gamma_1 \cap \Gamma_2 \cap \Gamma_3$, then it satisfies

$$369 \quad \begin{cases} |1 - \lambda(1 - c)| = \frac{\lambda}{2} \sqrt{\cos^2(2\theta_{N-r})c^2 - 2c + 1}, \\ 370 \quad \lambda c \cos(2\theta_{N-r}) - \lambda + 2 = 0. \end{cases}$$

371 On surfaces Γ_i , $i \in \{1, 2, 3\}$, the parameters $c \in (0, c^*)$ and $\lambda \in (0, 2]$ implies above
 372 equations only have one solution $c = \frac{1}{2}$ and $\lambda = \frac{4}{2 - \cos(2\theta_{N-r})}$. Thus, we have

$$373 \quad (2.10) \quad \Gamma_1 \cap \Gamma_2 \cap \Gamma_3 = \left\{ \left(\frac{1}{2}, \frac{4}{2 - \cos(2\theta_{N-r})}, -\frac{\cos(2\theta_{N-r})}{2 - \cos(2\theta_{N-r})} \right) \right\}.$$

374 Therefore, we know when $\theta_{N-r} \in (\frac{\pi}{4}, \frac{\pi}{2}]$, the minimum of $\max\{|\rho_1|, |\rho_2|, |\rho_3|\}$ for
 375 $c \in (0, c^*)$ and $\lambda \in (0, 2]$ is not greater than $-\frac{\cos(2\theta_{N-r})}{2 - \cos(2\theta_{N-r})}$. To deal with $c \in [c^*, 1)$, we
 376 need the following lemma.

377 **LEMMA 2.6.** *Assume ρ_1 and ρ_2 are functions of c and λ , for which the minimum*
 378 *can be attained. Then, the following inequality holds.*

$$379 \quad \min_{c, \lambda} \max\{|\rho_1|, |\rho_2|\} \geq \max\{\min_{c, \lambda} |\rho_1|, \min_{c, \lambda} |\rho_2|\}.$$

380 *Proof.* Assume the minimum of $\max\{|\rho_1|, |\rho_2|\}$ is achieved at (c_0, λ_0) . We have

- 381 i. If $|\rho_1(c_0, \lambda_0)| \geq |\rho_2(c_0, \lambda_0)|$, then $\min_{c, \lambda} \max\{|\rho_1|, |\rho_2|\} = |\rho_1(c_0, \lambda_0)| \geq$
 382 $\min_{c, \lambda} |\rho_1|$.
 383 ii. If $|\rho_1(c_0, \lambda_0)| < |\rho_2(c_0, \lambda_0)|$, then $\min_{c, \lambda} \max\{|\rho_1|, |\rho_2|\} = |\rho_2(c_0, \lambda_0)| >$
 384 $|\rho_1(c_0, \lambda_0)|$. Proof by contradiction: assume $\min_{c, \lambda} \max\{|\rho_1|, |\rho_2|\} < \min_{c, \lambda} |\rho_1|$,
 385 then it implies $|\rho_1(c_0, \lambda_0)| < \min_{c, \lambda} |\rho_1|$, which is impossible.

386 Thus, $\min_{c, \lambda} \max\{|\rho_1|, |\rho_2|\} \geq \min_{c, \lambda} |\rho_1|$. Similarly, $\min_{c, \lambda} \max\{|\rho_1|, |\rho_2|\} \geq \min_{c, \lambda} |\rho_2|$. \square

387 When $c \in [c^*, 1)$, the magnitude of ρ_2 and ρ_3 are equal, namely we only need to find
 388 suitable parameters c and λ such that the $\max\{|\rho_1|, |\rho_2|\}$ is reasonably small. It is
 389 easy to verify that, when $c \in [c^*, 1)$ and $\lambda \in (0, 2]$, the function ρ_1 is monotonically
 390 increasing with respect to c and monotonically decreasing with respect to λ . Thus,
 391 $\rho_1(c^*, 2) = 2c^* - 1 > 0$ gives $|\rho_1| = \rho_1$. Associated with λ greater or less than
 392 $-\frac{\cos(2\theta_{N-r})}{\sin^2 \theta_{N-r}}$, we have two cases.

393 1. When $\lambda \in (0, -\frac{\cos(2\theta_{N-r})}{\sin^2 \theta_{N-r}}]$, recall the monotonicity of ρ_1 , we have

$$394 \quad \min_{c \in [c^*, 1), \lambda \in (0, -\frac{\cos(2\theta_{N-r})}{\sin^2 \theta_{N-r}}]} |\rho_1| = \rho_1 \left(c^*, -\frac{\cos(2\theta_{N-r})}{\sin^2 \theta_{N-r}} \right)$$

$$395 \quad = 1 + \frac{\cos(2\theta_{N-r})}{\sin^2 \theta_{N-r}} \left(1 - \frac{1}{(\cos \theta_{N-r} + \sin \theta_{N-r})^2} \right) > \frac{1}{2} > -\frac{\cos(2\theta_{N-r})}{2 - \cos(2\theta_{N-r})}.$$

396 By Lemma 2.6, when the principal angle $\theta_{N-r} \in (\frac{\pi}{4}, \frac{\pi}{2}]$, we know

$$397 \quad \min_{c \in [c^*, 1), \lambda \in (0, -\frac{\cos(2\theta_{N-r})}{\sin^2 \theta_{N-r}}]} \max\{|\rho_1|, |\rho_2|\} > -\frac{\cos(2\theta_{N-r})}{2 - \cos(2\theta_{N-r})}.$$

400 Therefore, the common point of the three surfaces Γ_1 , Γ_2 , and Γ_3 in (2.10) is
 401 still a good choice.

402 2. When $\lambda \in (-\frac{\cos(2\theta_{N-r})}{\sin^2 \theta_{N-r}}, 2]$, define $\kappa = c\lambda^2 \sin^2 \theta_{N-r} - (1 - c \cos(2\theta_{N-r}))\lambda + 1$. We
 403 have $\frac{\partial \kappa}{\partial c} = \lambda(\lambda \sin^2 \theta_{N-r} + \cos(2\theta_{N-r})) > 0$, which implies κ is monotonically
 404 increasing with respect to c in the interval $[c^*, 1)$. Thus, for any $c \geq c^*$, the
 405 $|\rho_2(c, \lambda)| \geq |\rho_2(c^*, \lambda)|$ holds. Again, recall the monotonicity of ρ_1 , we obtain

$$406 \quad \min_{c \in [c^*, 1), \lambda \in (-\frac{\cos(2\theta_{N-r})}{\sin^2 \theta_{N-r}}, 2]} \max\{|\rho_1|, |\rho_2|\} = \min_{\lambda \in (-\frac{\cos(2\theta_{N-r})}{\sin^2 \theta_{N-r}}, 2]} \max\{|\rho_1(c^*, \lambda)|, |\rho_2(c^*, \lambda)|\}.$$

407 Since $|\rho_1(c^*, \lambda)| = 1 - \lambda(1 - c^*)$ and $|\rho_2(c^*, \lambda)| = |1 - \frac{\lambda}{1 + \cot \theta_{N-r}}|$, when $\theta_{N-r} \in$
 408 $(\frac{\pi}{4}, \frac{\pi}{2}]$, $\frac{1}{1 + \cot \theta_{N-r}} > 1 - c^*$, then the equation $|\rho_1(c^*, \lambda)| = |\rho_2(c^*, \lambda)|$ has one
 409 and only one root

$$410 \quad \lambda^* = \frac{2}{1 + \frac{1}{1 + \cot \theta_{N-r}} - \frac{1}{(\cos \theta_{N-r} + \sin \theta_{N-r})^2}}.$$

411 Therefore, we know when $\theta_{N-r} \in (\frac{\pi}{4}, \frac{\pi}{2}]$, the minimum of $\max\{|\rho_1|, |\rho_2|, |\rho_3|\}$
 412 for $c \in [c^*, 1)$ and $\lambda \in (-\frac{\cos(2\theta_{N-r})}{\sin^2 \theta_{N-r}}, 2]$ is not larger than $1 - \lambda^*(1 - c^*)$.

413 Next, let us consider the case $\theta_{N-r} \in (0, \frac{\pi}{4}]$. When $c \in (0, c^*)$ and $\lambda \in (0, 2]$, the
 414 discriminant $\Delta > 0$, namely the quadratic equation (2.9) has two real roots. Moreover,
 415 $|\rho_2| > |\rho_3|$ obviously. Thus, we only need to minimize the $\max\{|\rho_1|, |\rho_2|\}$. Define

$$416 \quad \tilde{\kappa} = \lambda c \cos(2\theta_{N-r}) - \lambda + 2 + \lambda \sqrt{\cos^2(2\theta_{N-r})c^2 - 2c + 1}.$$

417 Since for any $\theta_{N-r} \in (0, \frac{\pi}{4}]$, $c \in (0, c^*)$, and $\lambda \in (0, 2]$ the $\lambda c \cos(2\theta_{N-r}) - \lambda + 2 > 0$,
 418 we have $|\rho_2| = \frac{1}{2}\tilde{\kappa}$. From

$$419 \quad \frac{\partial \tilde{\kappa}}{\partial c} = \lambda \left(\cos(2\theta_{N-r}) + \frac{c \cos^2(2\theta_{N-r}) - 1}{\sqrt{\cos^2(2\theta_{N-r})c^2 - 2c + 1}} \right) \leq 0,$$

$$420 \quad \frac{\partial \tilde{\kappa}}{\partial \lambda} = c \cos(2\theta_{N-r}) - 1 + \sqrt{\cos^2(2\theta_{N-r})c^2 - 2c + 1} \leq 0,$$

422 we know the $\tilde{\kappa}$ is monotonically decreasing with respect to both c and λ . Thus $\tilde{\kappa}$ take
 423 minimum at $c = c^*$ and $\lambda = 2$. By Lemma 2.6, when the principal angle $\theta_{N-r} \in (0, \frac{\pi}{4}]$,
 424 we know

$$425 \quad (2.11) \quad \min_{c \in (0, c^*), \lambda \in (0, 2]} \max\{|\rho_1|, |\rho_2|\} \geq \min_{c \in (0, c^*), \lambda \in (0, 2]} |\rho_2| = \frac{1}{2}\tilde{\kappa}(c^*, 2) = c^* \cos 2\theta_{N-r}.$$

426 Notice, when $c = c^*$ and $\lambda = 2$, the magnitude of ρ_1 and ρ_2 can be simplified as
 427 $|\rho_1| = |2c^* - 1|$ and $|\rho_2| = c^* \cos 2\theta_{N-r}$, where $c^* = \frac{1}{(\cos \theta_{N-r} + \sin \theta_{N-r})^2}$. It is easy to
 428 check that $|\rho_2| > |\rho_1|$ holds for any $\theta_{N-r} \in (0, \frac{\pi}{4}]$. We have

$$(2.12) \quad \min_{c \in (0, c^*), \lambda \in (0, 2]} \max\{|\rho_1|, |\rho_2|\} \leq \max\{|\rho_1(c^*, 2)|, |\rho_2(c^*, 2)|\} = |\rho_2(c^*, 2)| = c^* \cos 2\theta_{N-r}.$$

431 From above (2.11) and (2.12), we obtain the minimum of $\max\{|\rho_1|, |\rho_2|, |\rho_3|\}$ equals
 432 $c^* \cos 2\theta_{N-r}$, which is achieved at $c = c^*$ and $\lambda = 2$. When $c \in [c^*, 2)$, following the
 433 similar argument as above, we can show $|\rho_1| = 1 - \lambda(1 - c)$, which is monotonically

434 increasing with respect to c and monotonically decreasing with respect to λ . In
 435 addition, we also have $|\rho_2| = |\rho_3|$ which is monotonically increasing with respect to
 436 c . Thus, we have

$$\begin{aligned}
 437 \quad \min_{c \in [c^*, 1], \lambda \in (0, 2]} \max\{|\rho_1|, |\rho_2|, |\rho_3|\} &= \min_{\lambda \in (0, 2]} \max\{|\rho_1(c^*, \lambda)|, |\rho_2(c^*, \lambda)|\} \\
 438 \quad &= \min_{\lambda \in (0, 2]} \frac{1}{2} \lambda c^* \cos(2\theta_{N-r}) - \frac{1}{2} \lambda + 1. \\
 439
 \end{aligned}$$

440 The last equality above is due to the fact the $|\rho_1(c^*, \lambda)| \leq |\rho_2(c^*, \lambda)|$ holds for any
 441 $\theta_{N-r} \in (0, \frac{\pi}{4}]$. From $\lambda c^* \cos(2\theta_{N-r}) - \lambda$ is monotonically decreasing with respect to
 442 λ , we know, in this case, the minimum equals $c^* \cos(2\theta_{N-r})$, which is taken at $c = c^*$
 443 and $\lambda = 2$.

444 To this end, let us make a summary of the parameter selection principle as follows.

- 445 1. When $\theta_{N-r} \in (\frac{3}{8}\pi, \frac{1}{2}\pi]$, a suitable choice of parameters are: $c = \frac{1}{2}$, $\lambda = \frac{4}{2 - \cos(2\theta_{N-r})}$.
- 446 The associated asymptotic linear convergence rate is governed by $-\frac{\cos(2\theta_{N-r})}{2 - \cos(2\theta_{N-r})}$.
- 447 2. When $\theta_{N-r} \in (\frac{1}{4}\pi, \frac{3}{8}\pi]$, a suitable choice of parameters are: $c = c^*$, $\lambda = \lambda^*$. The
 448 associated asymptotic linear convergence rate is governed by $1 - \lambda^*(1 - c^*)$.
- 449 3. When $\theta_{N-r} \in (0, \frac{1}{4}\pi]$, a suitable choice of parameters are: $c = c^*$, $\lambda = 2$. The
 450 associated asymptotic linear convergence rate is governed by $c^* \cos(2\theta_{N-r})$.

451 *Remark 2.7.* The exact value of the principal angle θ_{N-r} in (2.8) is unknown.
 452 But it is simple to estimate θ_{N-r} by counting the number of bad cells, e.g., let \hat{r} be
 453 the number of $u_i \notin [m, M]$ and use \hat{r} instead of r in (2.8) to compute θ_{N-r} . This gives
 454 a simple guideline (1.9) for choosing nearly optimal parameters, which is efficient in
 455 all our numerical tests as shown in Section 4.

456 *Remark 2.8.* In a large scale 3D problem, usually the ratio of bad cells with cell
 457 averages out of bound in the DG scheme is quite small. In such a case, we expect
 458 $r \ll N$, with which θ_{N-r} is very close to zero. In this case, by the discussions
 459 above, the convergence rate in Theorem 2.5 becomes $-\frac{\cos(2\theta_{N-r})}{2 - \cos(2\theta_{N-r})}$. If \hat{r} is also a good
 460 approximation to r , which is usually true in this context, then we get the rate (1.10).

461 With the guideline (1.9) for choosing nearly optimal parameters in (1.7a), we can
 462 use the two-step limiter as explained in Section 1.5 to enforce bounds of DG solutions.

463 **3. Application to phase-field equations.** One of the popular approaches for
 464 modeling multi-phase fluid flow in micro-to-millimeter pore structures is to use phase-
 465 field equations [15]. Efficient and accurate pore-scale fluid dynamics simulators have
 466 important applications in digital rock physics (DRP), which has been extensively used
 467 in the petroleum industry for optimizing enhanced oil recovery schemes.

468 **3.1. Mathematical model.** In an open bounded domain $\Omega \subset \mathbb{R}^d$ over a time
 469 interval $(0, T]$, the dimensionless CHNS equations are given by:

$$470 \quad (3.1a) \quad \partial_t \phi - \frac{1}{\text{Pe}} \nabla \cdot (\mathcal{M}(\phi) \nabla \mu) + \nabla \cdot (\phi \mathbf{v}) = 0 \quad \text{in } (0, T] \times \Omega,$$

$$471 \quad (3.1b) \quad \mu + \text{Cn}^2 \Delta \phi - \Phi'(\phi) = 0 \quad \text{in } (0, T] \times \Omega,$$

$$472 \quad (3.1c) \quad \partial_t \mathbf{v} + \mathbf{v} \cdot \nabla \mathbf{v} - \frac{2}{\text{Re}} \nabla \cdot \boldsymbol{\varepsilon}(\mathbf{v}) + \frac{1}{\text{ReCa}} \nabla p - \frac{3}{2\sqrt{2} \text{ReCaCn}} \mu \nabla \phi = 0 \quad \text{in } (0, T] \times \Omega,$$

$$473 \quad (3.1d) \quad \nabla \cdot \mathbf{v} = 0 \quad \text{in } (0, T] \times \Omega,$$

475 where ϕ , μ , \mathbf{v} , and p are order parameter, chemical potential, velocity, and pressure.
 476 The non-dimensional quantities Pe, Cn, Re, and Ca denote the Péclet number, Cahn
 477 number, Reynolds number, and capillary number, respectively. The strain tensor is
 478 given by $\boldsymbol{\varepsilon}(\mathbf{v}) = \frac{1}{2}(\nabla\mathbf{v} + (\nabla\mathbf{v})^T)$. The function \mathcal{M} denotes mobility. Typical choices of
 479 \mathcal{M} include the constant mobility $\mathcal{M}(\phi) = \mathcal{M}_0 > 0$, where \mathcal{M}_0 can be set to 1 after
 480 nondimensionalization, and the degenerate mobility $\mathcal{M}(\phi) = 1 - \phi^2$. The function
 481 Φ is a scalar potential, which is also called chemical energy density. Classical and
 482 widely used forms are the polynomial Ginzburg–Landau (GL) double well potential:
 483 $\Phi(\phi) = \frac{1}{4}(1 - \phi)^2(1 + \phi)^2$ and the Flory–Huggins (FH) logarithmic potential with
 484 parameters α and β : $\Phi(\phi) = \frac{\alpha}{2}((1 + \phi) \ln(\frac{1+\phi}{2}) + (1 - \phi) \ln(\frac{1-\phi}{2})) + \frac{\beta}{2}(1 - \phi^2)$.

485 We supplement (3.1) with initials $\phi = \phi^0$ and $\mathbf{v} = \mathbf{v}^0$ on $\{0\} \times \Omega$. Let \mathbf{n} denote
 486 the unit outward normal to domain Ω . We decompose the boundary $\partial\Omega$ into three
 487 disjoint subsets $\partial\Omega = \partial\Omega^{\text{wall}} \cup \partial\Omega^{\text{in}} \cup \partial\Omega^{\text{out}}$, where $\partial\Omega^{\text{wall}}$ denotes fluid–solid interface
 488 and $\partial\Omega^{\text{in}}$ and $\partial\Omega^{\text{out}}$ are inflow boundary and outflow boundary

$$489 \quad \partial\Omega^{\text{in}} = \{x \in \partial\Omega : \mathbf{v} \cdot \mathbf{n} < 0\} \quad \text{and} \quad \partial\Omega^{\text{out}} = \partial\Omega \setminus (\partial\Omega^{\text{wall}} \cup \partial\Omega^{\text{in}}).$$

490 We prescribe Dirichlet boundary conditions $\phi = \phi_D$ and $\mathbf{v} = \mathbf{v}_D$ on $(0, T] \times \partial\Omega^{\text{in}}$.
 491 For velocity, the no-slip boundary condition $\mathbf{v} = \mathbf{0}$ is used on $(0, T] \times \partial\Omega^{\text{wall}}$ and “do
 492 nothing” boundary condition $(2\boldsymbol{\varepsilon}(\mathbf{v}) - \frac{1}{\text{Ca}}p\mathbf{I})\mathbf{n} = \mathbf{0}$ is applied on $(0, T] \times \partial\Omega^{\text{out}}$. Wet-
 493 tability is modeled by a contact angle ϑ that is enforced by: $\nabla\phi \cdot \mathbf{n} = -\frac{2\sqrt{2}\cos(\vartheta)}{3\text{Cn}}g'(\phi)$
 494 on $(0, T] \times (\partial\Omega^{\text{wall}} \cup \partial\Omega^{\text{out}})$, where the function g is a blending function. The closed-
 495 form expression of g depends on the choice of chemical energy density [4]. For the
 496 Ginzburg–Landau potential, we have $g(\phi) = \frac{1}{4}(\phi^3 - 3\phi + 2)$. In addition, we employ
 497 the homogeneous Neumann boundary condition $\mathcal{M}(\phi)\nabla\mu \cdot \mathbf{n} = 0$ on $(0, T] \times \partial\Omega$ to
 498 ensure the global mass conservation.

499 The order parameter ϕ is the difference between the mass fraction ϕ_A and ϕ_B of
 500 the phase A and phase B. With constraint $\phi_A + \phi_B = 1$ for a two-component mixture
 501 as well as mass fractions belonging to $[0, 1]$, a physically meaningful range of the order
 502 parameter field is $[-1, 1]$. The Cahn–Hilliard equation with the degenerate mobility
 503 or with the logarithmic potential enjoys bound-preserving property [41]. However,
 504 for constant mobility with GL polynomial potential, the analytical solution of Cahn–
 505 Hilliard equation is not bound-preserving [2]. For a given initial data $\phi^0 \in [-1, 1]$, it is
 506 an open question whether the solution of a fully coupled CHNS system should have a
 507 bounded order parameter in $[-1, 1]$. On the other hand, empirically we would expect
 508 a reasonable solution, e.g., the discrete order parameter field, should be bounded by
 509 -1 and 1 for any time $t > 0$.

510 **3.2. Time discretization.** The CHNS equations form a highly nonlinear cou-
 511 pled system. One of the popular approaches of constructing efficient numerical algo-
 512 rithms for large-scale simulations in complex computational domains is to use splitting
 513 methods, e.g., to decouple the mass and momentum equations and to further split
 514 the convection from the incompressibility constraint [37]. Also, see [21, 19] for an
 515 overview of the splitting methods for time-dependent incompressible flows.

516 We uniformly partition the interval $[0, T]$ into N_{st} subintervals. Let τ denote the
 517 time step size. For the chemical energy density, we adopt a convex–concave decom-
 518 position of the form $\Phi = \Phi_+ + \Phi_-$, where the convex part Φ_+ is treated time implicitly
 519 and the concave part Φ_- is treated time explicitly. For the nonlinear convection
 520 $\mathbf{v} \cdot \nabla\mathbf{v}$, the form $\mathcal{C}(\cdot, \cdot)$ is a semi-discretization that satisfies a positivity property, see
 521 the equation (12) in [27]. For any $1 \leq n \leq N_{\text{st}}$, our first-order time discretization

522 algorithm consists of the following steps:

523 Step 1. Given $(\phi^{n-1}, \mathbf{w}^{n-1})$, compute (ϕ^n, μ^n) such that

$$\begin{aligned}
 524 \quad \phi^n - \frac{\tau}{\text{Pe}} \nabla \cdot (\mathcal{M}(\phi^{n-1}) \nabla \mu^n) + \tau \nabla \cdot (\phi^n \mathbf{w}^{n-1}) &= \phi^{n-1} && \text{in } \Omega, \\
 525 \quad -\mu^n - \text{Cn}^2 \Delta \phi^n + \Phi_+'(\phi^n) &= -\Phi_-'(\phi^{n-1}) && \text{in } \Omega.
 \end{aligned}$$

527 Step 2. Given $(\phi^n, \mu^n, \mathbf{v}^{n-1}, p^{n-1}, \psi^{n-1})$, compute \mathbf{v}^n such that

$$\begin{aligned}
 528 \quad \mathbf{v}^n + \tau \mathbf{C}(\mathbf{v}^{n-1}, \mathbf{v}^n) - \frac{2\tau}{\text{Re}} \nabla \cdot \boldsymbol{\varepsilon}(\mathbf{v}^n) &= \mathbf{v}^{n-1} \\
 529 \quad -\frac{\tau}{\text{ReCa}} \nabla(p^{n-1} + \psi^{n-1}) + \frac{3\tau}{2\sqrt{2} \text{ReCaCn}} \mu^n \nabla \phi^n & \quad \text{in } \Omega. \\
 530
 \end{aligned}$$

531 Step 3. Given \mathbf{v}^n , compute ψ^n such that

$$\begin{aligned}
 532 \quad -\Delta \psi^n &= -\frac{\text{ReCa}}{\tau} \nabla \cdot \mathbf{v}^n && \text{in } \Omega. \\
 533
 \end{aligned}$$

534 Step 4. Given $(\mathbf{v}^n, p^{n-1}, \psi^n)$, compute (\mathbf{w}^n, p^n) such that

$$\begin{aligned}
 535 \quad \mathbf{w}^n &= \mathbf{v}^n - \frac{\tau}{\text{ReCa}} \nabla \psi^n, \\
 536 \quad p^n &= p^{n-1} + \psi^n - \sigma_\chi \text{Ca} \nabla \cdot \mathbf{v}^n. \\
 537
 \end{aligned}$$

538 The parameter σ_χ is equal to $\frac{2}{d}$, namely, we use $\sigma_\chi = \frac{2}{3}$ for our numerical simulations
 539 in three dimensions. To start time marching, we set $p^0 = 0$ and $\psi^0 = 0$. The functions
 540 ϕ^0 and $\mathbf{w}^0 = \mathbf{v}^0$ are given initial data.

541 *Remark 3.1.* The above scheme is a combination of the convex splitting approach
 542 for the Cahn–Hilliard equation with the classical rotational pressure-correction algo-
 543 rithm (see Section 3.4 in [21]) for the Navier–Stokes equations. More precisely, Step 2
 544 to Step 4 can be rewritten as follows:

$$\begin{aligned}
 545 \quad \frac{1}{\tau} (\mathbf{v}^n - \mathbf{w}^{n-1}) + \mathbf{C}(\mathbf{v}^{n-1}, \mathbf{v}^n) - \frac{2}{\text{Re}} \nabla \cdot \boldsymbol{\varepsilon}(\mathbf{v}^n) &= -\frac{1}{\text{ReCa}} \nabla p^{n-1} + \frac{3}{2\sqrt{2} \text{ReCaCn}} \mu^n \nabla \phi^n, \\
 546 \quad \begin{cases} \frac{1}{\tau} (\mathbf{w}^n - \mathbf{v}^n) + \frac{1}{\text{ReCa}} \nabla \psi^n = 0, \\ \nabla \cdot \mathbf{w}^n = 0, \end{cases} & \quad \psi^n = p^n - p^{n-1} + \sigma_\chi \text{Ca} \nabla \cdot \mathbf{v}^n. \\
 547
 \end{aligned}$$

548 We use \mathbf{w}^{n-1} , instead of \mathbf{v}^{n-1} , in the advection term in Step 1, since $\nabla \cdot \mathbf{w}^{n-1} = 0$.

549 For the sake of simplicity, we only presented a first-order version of the scheme,
 550 although high-order version can be constructed accordingly. On the other hand, it
 551 is also possible to construct energy dissipating schemes as in [38]. Since our focus in
 552 this paper is in preserving bounds for a DG spacial discretization, we employ a simple
 553 time-marching strategy.

554 **3.3. Space discretization.** Decoupled splitting algorithms combined with interi-
 555 or penalty DG spatial formations have been constructed to solve various CHNS mod-
 556 els in large-scale complex-domain DRP simulations [15, 28, 30]. Also, see [29, 32, 33]
 557 for solvability, stability, and optimal error estimates on using DG with decoupled split-
 558 ting schemes for CHNS equations and viscous incompressible flow. Here, we briefly
 559 review the fully discrete scheme.

560 Let $\mathcal{T}_h = \{E_i\}$ be a family of conforming nondegenerate (regular) meshes of the
 561 domain Ω with maximum element diameter h . Let Γ_h be the set of interior faces. For
 562 each interior face $e \in \Gamma_h$ shared by elements E_{i^-} and E_{i^+} , with $i^- < i^+$, we define a
 563 unit normal vector \mathbf{n}_e that points from E_{i^-} into E_{i^+} . For a boundary face, $e \subset \partial\Omega$,
 564 the normal vector \mathbf{n}_e is taken to be the unit outward vector to $\partial\Omega$. Let $\mathbb{P}_k(E_i)$ denote
 565 the set of all polynomials of degree at most k on an element E_i . Define the broken
 566 polynomial spaces X_h and \mathbf{X}_h , for any $k \geq 1$,

$$567 \quad X_h = \{\chi_h \in L^2(\Omega) : \chi_h|_{E_i} \in \mathbb{P}_k(E_i), \forall E_i \in \mathcal{T}_h\},$$

$$568 \quad \mathbf{X}_h = \{\boldsymbol{\theta}_h \in L^2(\Omega)^d : \boldsymbol{\theta}_h|_{E_i} \in \mathbb{P}_k(E_i)^d, \forall E_i \in \mathcal{T}_h\}.$$

570 The average and jump for any scalar quantity χ on a boundary face coincide with its
 571 trace; and on interior faces they are defined by

$$572 \quad \{\!\!\{ \chi \}\!\!\}_e = \frac{1}{2} \chi|_{E_{i^-}} + \frac{1}{2} \chi|_{E_{i^+}}, \quad \llbracket \chi \rrbracket|_e = \chi|_{E_{i^-}} - \chi|_{E_{i^+}}, \quad \forall e = \partial E_{i^-} \cap \partial E_{i^+}.$$

573 The related definitions for any vector quantity are similar. For more details see [36].

574 Let $(\cdot, \cdot)_{\mathcal{O}}$ denote the L^2 inner product over \mathcal{O} . For instance, on any face e the L^2
 575 inner product is denoted by $(\cdot, \cdot)_e$. We make use of the following compact notation
 576 for the L^2 inner product on the interior and boundary faces

$$577 \quad (\cdot, \cdot)_{\mathcal{O}} = \sum_{e \in \mathcal{O}} (\cdot, \cdot)_e, \quad \text{where } \mathcal{O} = \Gamma_h, \partial\Omega, \partial\Omega^{\text{in}}, \partial\Omega^{\text{out}}, \dots$$

578 For convenience, we omit the subscript when $\mathcal{O} = \Omega$, namely denote $(\cdot, \cdot) = (\cdot, \cdot)_{\Omega}$. We
 579 still use ∇ and $\nabla \cdot$ to denote the broken gradient and broken divergence.

580 For completeness, let us recall the DG forms below and we skip their derivation.
 581 Associated with the advection term $\nabla \cdot (\phi \mathbf{w})$ and the convection term $\mathbf{v} \cdot \nabla \mathbf{z}$, we define

$$582 \quad a_{\text{adv}}(\phi, \mathbf{w}, \chi) = -(\phi, \mathbf{w} \cdot \nabla \chi) + (\phi^\uparrow \{\!\!\{ \mathbf{w} \cdot \mathbf{n}_e \}\!\!\}, \llbracket \chi \rrbracket)_{\Gamma_h},$$

$$583 \quad a_{\text{conv}}(\mathbf{v}; \mathbf{z}, \boldsymbol{\theta}) = (\mathbf{v} \cdot \nabla \mathbf{z}, \boldsymbol{\theta}) + \frac{1}{2} (\nabla \cdot \mathbf{v}, \mathbf{z} \cdot \boldsymbol{\theta})$$

$$584 \quad - \frac{1}{2} (\llbracket \mathbf{v} \cdot \mathbf{n}_e \rrbracket, \{\!\!\{ \mathbf{z} \cdot \boldsymbol{\theta} \}\!\!\})_{\Gamma_h \cup \partial\Omega^{\text{in}}} + \sum_{E \in \mathcal{T}_h} (\{\!\!\{ \mathbf{v} \}\!\!\} \cdot \mathbf{n}_E, (\mathbf{z}^{\text{int}} - \mathbf{z}^{\text{ext}}) \cdot \boldsymbol{\theta}^{\text{int}})_{\partial E_-^v}.$$

$$585$$

586 The superscript int (resp. ext) refers to the trace of a function on a face of E coming
 587 from the interior (resp. exterior). The set ∂E_-^v is the upwind part of ∂E , defined by
 588 $\partial E_-^v = \{\mathbf{x} \in \partial E : \{\!\!\{ \mathbf{v} \}\!\!\} \cdot \mathbf{n}_E < 0\}$, where \mathbf{n}_E is the unit outward normal vector to E [18].
 589 The upwind quantity ϕ^\uparrow on an interior face e is evaluated by

$$590 \quad \phi^\uparrow|_{e \in \Gamma_h} = \begin{cases} \phi|_{E_{i^-}} & \text{if } \{\!\!\{ \mathbf{w} \}\!\!\} \cdot \mathbf{n}_e \geq 0, \\ \phi|_{E_{i^+}} & \text{if } \{\!\!\{ \mathbf{w} \}\!\!\} \cdot \mathbf{n}_e < 0. \end{cases}$$

591 Associated with the operator $-\nabla \cdot (z \nabla \xi)$, we define

$$592 \quad a_{\text{diff}}(z; \xi, \chi) = (z \nabla \xi, \nabla \chi) - (\{\!\!\{ z \nabla \xi \cdot \mathbf{n}_e \}\!\!\}, \llbracket \chi \rrbracket)_{\Gamma_h}$$

$$593 \quad - (\{\!\!\{ z \nabla \chi \cdot \mathbf{n}_e \}\!\!\}, \llbracket \xi \rrbracket)_{\Gamma_h} + \frac{\sigma}{h} (\llbracket \xi \rrbracket, \llbracket \chi \rrbracket)_{\Gamma_h}.$$

$$594$$

595 Associated with the Laplace operator $-\Delta\xi$ (for terms $-\Delta\phi$ and $-\Delta\psi$), we define

$$\begin{aligned}
 596 \quad -\Delta\xi + \text{Dirichlet on } \partial\Omega^{\text{in}} &\rightsquigarrow a_{\text{diff,in}}(\xi, \chi) = a_{\text{diff}}(1; \xi, \chi) - (\nabla\xi \cdot \mathbf{n}_e, \chi)_{\partial\Omega^{\text{in}}} \\
 &\quad - (\nabla\chi \cdot \mathbf{n}_e, \xi)_{\partial\Omega^{\text{in}}} + \frac{\sigma}{h}(\xi, \chi)_{\partial\Omega^{\text{in}}}, \\
 597 \\
 598 \quad -\Delta\xi + \text{Dirichlet on } \partial\Omega^{\text{out}} &\rightsquigarrow a_{\text{diff,out}}(\xi, \chi) = a_{\text{diff}}(1; \xi, \chi) - (\nabla\xi \cdot \mathbf{n}_e, \chi)_{\partial\Omega^{\text{out}}} \\
 &\quad - (\nabla\chi \cdot \mathbf{n}_e, \xi)_{\partial\Omega^{\text{out}}} + \frac{\sigma}{h}(\xi, \chi)_{\partial\Omega^{\text{out}}}. \\
 599 \\
 600
 \end{aligned}$$

601 Associated with the diffusion term $-2\nabla \cdot \boldsymbol{\varepsilon}(\mathbf{v})$, we define

$$\begin{aligned}
 602 \\
 603 \quad a_{\text{ellip}}(\mathbf{v}, \boldsymbol{\theta}) &= 2(\boldsymbol{\varepsilon}(\mathbf{v}), \boldsymbol{\varepsilon}(\boldsymbol{\theta})) - 2(\{\boldsymbol{\varepsilon}(\mathbf{v})\mathbf{n}_e\}, \llbracket \boldsymbol{\theta} \rrbracket)_{\Gamma_h} - 2(\{\boldsymbol{\varepsilon}(\boldsymbol{\theta})\mathbf{n}_e\}, \llbracket \mathbf{v} \rrbracket)_{\Gamma_h} \\
 604 &\quad + \frac{\sigma}{h}(\llbracket \mathbf{v} \rrbracket, \llbracket \boldsymbol{\theta} \rrbracket)_{\Gamma_h} - 2(\boldsymbol{\varepsilon}(\mathbf{v})\mathbf{n}_e, \boldsymbol{\theta})_{\partial\Omega^{\text{in}}} - 2(\boldsymbol{\varepsilon}(\boldsymbol{\theta})\mathbf{n}_e, \mathbf{v})_{\partial\Omega^{\text{in}}} + \frac{\sigma}{h}(\mathbf{v}, \boldsymbol{\theta})_{\partial\Omega^{\text{in}}}. \\
 605
 \end{aligned}$$

606 The remaining forms in the right-hand sides of the discrete equations account for the
607 boundary conditions (see b_{diff} and b_{vel}) and the pressure and potential (see b_{pres}):

$$\begin{aligned}
 608 \quad b_{\text{diff}}(\xi, \chi) &= -(\phi_{\text{D}}, \nabla\chi \cdot \mathbf{n}_e)_{\partial\Omega^{\text{in}}} + \frac{\sigma}{h}(\phi_{\text{D}}, \chi)_{\partial\Omega^{\text{in}}} - \frac{2\sqrt{2}\delta \cos(\vartheta)}{3\text{Cn}}(g'(\xi), \chi)_{\partial\Omega^{\text{wall}} \cup \partial\Omega^{\text{out}}}, \\
 609 \quad b_{\text{pres}}(p, \psi, \boldsymbol{\theta}) &= -(p, \nabla \cdot \boldsymbol{\theta}) + (\{p\}, \llbracket \boldsymbol{\theta} \cdot \mathbf{n}_e \rrbracket)_{\Gamma_h \cup \partial\Omega} + (\nabla\psi, \boldsymbol{\theta}), \\
 610 \quad b_{\text{vel}}(\boldsymbol{\theta}) &= -\frac{3}{2}(\mathbf{v}_{\text{D}} \cdot \mathbf{n}, \mathbf{v}_{\text{D}} \cdot \boldsymbol{\theta})_{\partial\Omega^{\text{in}}} - \frac{2}{\text{Re}}(\boldsymbol{\varepsilon}(\boldsymbol{\theta})\mathbf{n}_e, \mathbf{v}_{\text{D}})_{\partial\Omega^{\text{in}}} + \frac{\sigma}{h\text{Re}}(\mathbf{v}_{\text{D}}, \boldsymbol{\theta})_{\partial\Omega^{\text{in}}}. \\
 611
 \end{aligned}$$

612 In b_{diff} , the parameter δ is a scalar field that equals the constant one for smooth solid
613 boundaries only and that otherwise corrects the numerical impact of the jaggedness
614 of the solid boundaries obtained from micro-CT scanning. The derivation of this
615 boundary condition and the wettability model can be found in [16].

616 For any $1 \leq n \leq N_{\text{st}}$, our fully discrete scheme for solving the CHNS equations
617 (3.1) is as follows.

618 **Algorithm CHNS.** At time t^n , given scalar functions $\phi_h^{n-1}, p_h^{n-1}, \psi_h^{n-1}$ in X_h and
619 vector functions $\mathbf{v}_h^{n-1}, \mathbf{w}_h^{n-1}$ in \mathbf{X}_h .

620 Step 1. Compute $\phi_h^n, \mu_h^n \in X_h$, such that for all $\chi_h \in X_h$,

$$\begin{aligned}
 621 \quad (\phi_h^n, \chi_h) + \frac{\tau}{\text{Pe}} a_{\text{diff}}(\mathcal{M}(\phi_h^{n-1}); \mu_h^n, \chi_h) + \tau a_{\text{adv}}(\phi_h^n, \mathbf{w}_h^{n-1}, \chi_h) \\
 622 \quad \quad \quad = (\phi_h^{n-1}, \chi_h) + \tau(\phi_{\text{D}} \mathbf{w}_h^{n-1} \cdot \mathbf{n}_e, \chi_h)_{\partial\Omega^{\text{in}}}, \\
 623 \quad -(\mu_h^n, \chi_h) + \text{Cn}^2 a_{\text{diff,in}}(\phi_h^n, \chi_h) + (\Phi_+'(\phi_h^n), \chi_h) \\
 624 \quad \quad \quad = \text{Cn}^2 b_{\text{diff}}(\phi_h^{n-1}, \chi_h) - (\Phi_-'(\phi_h^{n-1}), \chi_h). \\
 625
 \end{aligned}$$

626 Step 2. Compute $\mathbf{v}_h^n \in \mathbf{X}_h$, such that for all $\boldsymbol{\theta}_h \in \mathbf{X}_h$,

$$\begin{aligned}
 627 \\
 628 \quad (\mathbf{v}_h^n, \boldsymbol{\theta}_h) + \tau a_{\text{conv}}(\mathbf{v}_h^{n-1}, \mathbf{v}_h^n, \boldsymbol{\theta}_h) + \frac{\tau}{\text{Re}} a_{\text{ellip}}(\mathbf{v}_h^n, \boldsymbol{\theta}_h) = (\mathbf{v}_h^{n-1}, \boldsymbol{\theta}_h) \\
 629 \quad \quad \quad - \frac{\tau}{\text{ReCa}} b_{\text{pres}}(p_h^{n-1}, \psi_h^{n-1}, \boldsymbol{\theta}_h) + \frac{3\tau}{2\sqrt{2}\text{ReCaCn}} (\mu_h^n \nabla \phi_h^n, \boldsymbol{\theta}_h) + \tau b_{\text{vel}}(\boldsymbol{\theta}_h). \\
 630
 \end{aligned}$$

631 Step 3. Compute $\psi_h^n \in X_h$, such that for all $\chi_h \in X_h$,

$$632 \quad a_{\text{diff,out}}(\psi_h^n, \chi_h) = -\frac{\text{ReCa}}{\tau} (\nabla \cdot \mathbf{v}_h^n, \chi_h).$$

633 Step 4. Compute $\mathbf{w}_h^n \in \mathbf{X}_h$ and $p_h^n \in X_h$, such that for all $\boldsymbol{\theta} \in \mathbf{X}_h$ and $\chi_h \in X_h$,

$$634 \quad (\mathbf{w}_h^n, \boldsymbol{\theta}_h) + \sigma_{\text{div}}(\nabla \cdot \mathbf{w}_h^n, \nabla \cdot \boldsymbol{\theta}_h) = (\mathbf{v}_h^n, \boldsymbol{\theta}_h) - \frac{\tau}{\text{ReCa}}(\nabla \psi_h^n, \boldsymbol{\theta}_h),$$

$$635 \quad (p_h^n, \chi_h) = (p_h^{n-1}, \chi_h) + (\psi_h^n, \chi_h) - \sigma_\chi \text{Ca}(\nabla \cdot \mathbf{v}_h^n, \chi_h).$$

637 For the initial conditions, we set $p_h^0 = \psi_h^0 = 0$, $\mathbf{w}_h^0 = \mathbf{v}_h^0$; we compute ϕ_h^0 from the
638 L^2 projection of ϕ^0 followed with Zhang–Shu limiter and we obtain \mathbf{v}_h^0 from the L^2
639 projection of \mathbf{v}^0 .

640 To obtain a bound-preserving discrete order parameter field, at each time step
641 after finishing computing Step 1 in the Algorithm CHNS, we apply the two-stage
642 limiting strategy, see Section 1.5, to postprocess discrete order parameter ϕ_h^n . For the
643 simulations in Section 4, we choose $m = -1$ and $M = 1$.

644 **4. Numerical experiments.** In this section, we first verify the high order ac-
645 curacy of our cell average limiter (1.7) for a manufactured smooth solution. Then
646 we verify the efficiency of the limiter (1.7) when using the parameters (1.9) on some
647 representative physical simulations including spinodal decomposition, flows in micro
648 structure, and merging droplets.

649 We use \mathbb{P}_2 scheme, e.g., discontinuous piecewise quadratic polynomials for space
650 approximation, on cubic partitions of 3D domains. More details can be found in [14].

651 The penalty parameters for all tests are as follows. We use $\sigma = 8$ on Γ_h for a_{diff} ;
652 $\sigma = 16$ on $\partial\Omega$ for $a_{\text{diff},\text{in}}$ and $a_{\text{diff},\text{out}}$; $\sigma = 32$ on Γ_h and $\sigma = 64$ on $\partial\Omega^{\text{in}}$ for a_{ellip} . In
653 addition, we set tolerance $\epsilon = 10^{-13}$ to terminate Douglas–Rachford iterations.

654 **4.1. Accuracy test.** We use the manufactured solution method on domain $\Omega =$
655 $(0, 1)^3$ with end time $T = 0.1$ to test the spatial order of convergence for our cell average
656 limiter (1.7).

657 To trigger the cell average limiter (1.7), e.g., produce a fully discrete solution
658 with cell average out of $[-1, 1]$ at each time step, we use constant mobility with GL
659 polynomial potential and choose the prescribed order parameter field as an expres-
660 sion of a cosine function to power eight, as follows: $\phi = 1 - 2 \cos^8(t + \frac{2\pi}{3}(x + y + z))$.
661 The chemical potential μ is an intermediate variable, which value is derived by the
662 order parameter ϕ . The prescribed velocity and pressure fields are taken from the
663 Beltrami flow [32], which enjoys the property that the nonlinear convection is bal-
664 anced by the pressure gradient and the velocity is parallel to vorticity. We have

$$665 \quad \mathbf{v} = \begin{bmatrix} -e^{-t+x} \sin(y+z) - e^{-t+z} \cos(x+y) \\ -e^{-t+y} \sin(x+z) - e^{-t+x} \cos(y+z) \\ -e^{-t+z} \sin(x+y) - e^{-t+y} \cos(x+z) \end{bmatrix} \text{ and } p = -e^{-2t}(e^{x+z} \sin(y+z) \cos(x+y) +$$

666 $e^{x+y} \sin(x+z) \cos(y+z) + e^{y+z} \sin(x+y) \cos(x+z) + \frac{1}{2}e^{2x} + \frac{1}{2}e^{2y} + \frac{1}{2}e^{2z} - \overline{p^0})$, where
667 $\overline{p^0} = 7.63958172715414$ guarantees zero average pressure over Ω for any $t > 0$ up to
668 round-off error. The initial conditions and Dirichlet boundary condition for velocity
669 are imposed by above manufactured solutions. For order parameter and chemical
670 potential, we apply Neumann boundary condition. In addition, the right-hand side
671 terms is evaluated by the prescribed solution.

672 Let us estimate the spatial rates of convergence by computing solutions on a
673 sequence of uniformly refined meshes with fixed time step size $\tau = 10^{-4}$. In our
674 experiments, the time step size is small enough such that the spatial error dominates.
675 We choose $\text{Re} = 1$, $\text{Ca} = 1$, $\text{Pe} = 1$, $\text{Cn} = 1$, and the contact angle $\vartheta = 90^\circ$ on
676 $\partial\Omega$. If err_h denotes the error on a mesh with resolution h , then the rate is given by
677 $\ln(\text{err}_h/\text{err}_{h/2})/\ln 2$.

678 We compare the L_h^2 rate and the L_h^∞ rate of order parameter in three scenarios: not
 679 applying any limiter, only applying the cell average limiter (1.7), and applying both
 680 limiters (1.7) and (1.8). In those applied cell average limiter (1.7) cases, the limiter
 681 is triggered at each time step, see Figure 1 for the ratio of the number of trouble cells
 682 to the number of total elements. The convergence of our original DG scheme without
 683 applying any limiter is optimal, see the top rows in Table 1. The middle and bottom
 684 rows in Table 1 show optimal convergence of the cases that only apply cell average
 685 limiter (1.7) and apply both cell average limiter (1.7) and Zhang–Shu limiter (1.8).
 686 Our limiting strategy preserves high order accuracy. We emphasize that DG methods
 687 with only the Zhang-Shu limiter will produce cell averages outside of the range $[-1, 1]$
 688 for this particular test.

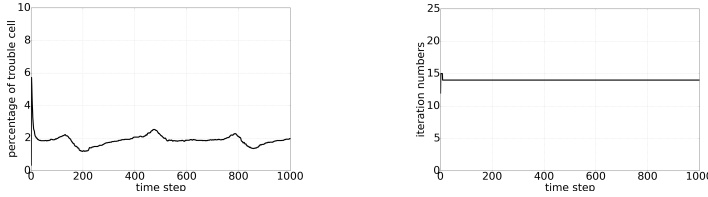


FIG. 1. *The performance of limiting strategy in the accuracy test of applying both limiters (1.7) and (1.8) with mesh resolution $h = 1/2^5$. Left: the percentage of trouble cells at each time step for the cell average limiter (1.7). Right: the number of Douglas–Rachford iterations at each time step. For each time step, at most 15 iterations are needed for (1.7a)*

	h	$\ \phi_h^{N_{st}} - \phi(T)\ _{L_h^2}$	rate	$\ \phi_h^{N_{st}} - \phi(T)\ _{L_h^\infty}$	rate
no limiter	$1/2^2$	2.034 E-1	—	5.636 E-1	—
	$1/2^3$	4.903 E-2	2.053	1.400 E-1	2.009
	$1/2^4$	5.714 E-3	3.101	2.731 E-2	2.358
	$1/2^5$	4.833 E-4	3.564	4.699 E-3	2.548
DR	$1/2^2$	2.053 E-1	—	5.826 E-1	—
	$1/2^3$	4.954 E-2	2.051	1.485 E-1	1.972
	$1/2^4$	5.720 E-3	3.115	2.799 E-2	2.408
	$1/2^5$	4.834 E-4	3.565	4.734 E-3	2.564
DR+ZS	$1/2^2$	2.872 E-1	—	7.631 E-1	—
	$1/2^3$	5.970 E-2	2.266	2.561 E-1	1.575
	$1/2^4$	7.181 E-3	3.057	3.926 E-2	2.706
	$1/2^5$	4.833 E-4	3.893	4.734 E-3	3.052

TABLE 1

Errors and spatial convergence rates of order parameter. Top: the original DG scheme without applying any limiters. Middle: only apply the cell average limiter (1.7) (DR). Bottom: apply both of the cell average limiter (1.7) and Zhang–Shu limiter (1.8).

689 **4.2. Spinodal decomposition.** Spinodal decomposition is a phase separation
 690 mechanism, by which an initially thermodynamically unstable homogeneous mixture
 691 spontaneously decomposes into two separated phases that are more thermodynamically
 692 favorable. The spinodal decomposition test is a widely used benchmark for

693 validating CHNS simulators. In this part, we employ the degenerate mobility with
694 GL polynomial potential.

695 We define a trefoil-shaped pipe, which is a set of points whose distance away
696 from the following parametric curve is less than 0.09. A trefoil knot: $x(t) = \frac{1}{8}(\cos t +$
697 $2 \cos 2t) + \frac{1}{2}$, $y(t) = \frac{1}{8}(\sin t - 2 \sin 2t) + \frac{1}{2}$, and $z(z) = \frac{1}{4} \sin 3t + \frac{1}{2}$, where $t \in [0, 2\pi]$. Let
698 us uniformly partition the unit cube $(0, 1)^3$ into cubic cells with the mesh resolution
699 $h = 1/100$. A cell is marked as fluid if its center is in the above pipe, otherwise is
700 marked as solid. The computational domain Ω is defined as the union of all fluid cells.
701 We consider a closed system, i.e., $\partial\Omega = \partial\Omega^{\text{wall}}$. The initial order parameter field is
702 generated by sampling numbers from a discrete uniform distribution, $c^0|_{E_i} \sim U\{-1, 1\}$,
703 and the initial velocity field is taken to be zero. We take the time step size $\tau = 1 \times 10^{-3}$.
704 For physical parameters, we choose $\text{Re} = 1$, $\text{Ca} = 0.1$, $\text{Pe} = 1$, $\text{Cn} = h$, and the contact
705 angle $\vartheta = 90^\circ$ on $\partial\Omega$.

706 Figure 2 shows snapshots of the order parameter field. We employ a rainbow color
707 scale that maps the values in $[-1, 1]$ from transparent blue to non-transparent red
708 for plotting the order parameter field. The center of the diffusive interface is colored
709 green. We observe that the homogeneous mixture decomposes into two separate phases.
710 With a neutral wall, i.e., the contact angle $\vartheta = 90^\circ$, in the final stage of the
711 simulation, each of the two phases occupies several disjoint sections of the domain.
712 The interfaces are perpendicular to the solid surface. Our limiters remove overshoots
713 and undershoots. The global mass is conserved, see the left subfigure of Figure 3.

714 The middle subfigure of Figure 3 records the number of iterations of the Douglas–
715 Rachford algorithm on each time step. To measure the convergence rate, we run
716 the Douglas–Rachford algorithm for 10^3 iterations with a very small tolerance to
717 approximate \mathbf{y}^* and \mathbf{x}^* numerically. Then we plot $\|\mathbf{y}^k - \mathbf{y}^*\|_2$ and $\|\mathbf{x}^k - \mathbf{x}^*\|_2$. The
718 right subfigure of Figure 3 shows asymptotic linear convergence rates at the selected
719 time step 128. We see the convergence rates match our analysis in Theorem 2.5. In
720 addition, we check the convergence rates on all of the rest steps that match with our
analysis.

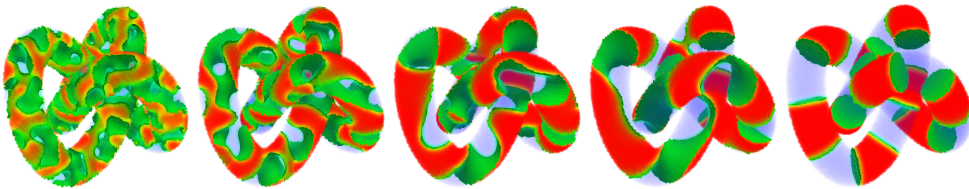


FIG. 2. Selected snapshots at time steps 2^n , where $n = 3, 5, \dots, 11$. 3D views of the evolution of order parameter field.

721

722 **4.3. Micro structure simulations.** This example involves large Péclet flows in
723 a microfluidic device, making it an interesting test for validating our bound-preserving
724 scheme in simulating advection-dominated CHNS problems. In this part, we use the
725 constant mobility with GL polynomial potential.

726 The microstructure image is a set of $334 \times 210 \times 10$ cubic cells of resolution
727 $h = 1/350$. Analogous to the lab experiment setup, we add a buffer of $16 \times 210 \times 70$ cells
728 to the left side. The pore space together with the buffer region form our computational
729 domain Ω , see Figure 4. We refer to phase A the bulk phase with order parameter
730 equals to $+1$ and phase B the bulk phase with order parameter equals to -1 . The
731 buffer zone is initially filled with phase A and the microstructure is initially filled with

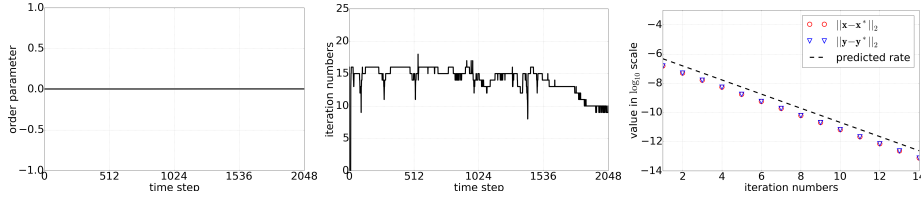


FIG. 3. *Left: the average of order parameter at each time step, which shows the conservation is preserved. Middle: the number of Douglas–Rachford iterations at each time step. Right: the asymptotic linear convergence at time step 128. The predicted rate is the rate given in Theorem 2.5.*

732 phase B, respectively. The initial velocity field is taken to be zero. The left boundary
 733 of Ω is inflow, the right boundary of Ω is outflow, and the rest boundaries of Ω are
 734 fluid–solid interfaces. On the inflow boundary, we prescribe $\phi_D = 1$, e.g., the phase
 735 A is injected, and $\mathbf{v}_D = \frac{10000}{9}(y - 0.2)(y - 0.8)(z - 0.4)(z - 0.6)$. We take time step
 736 size $\tau = 5 \times 10^{-4}$. For physical parameters, we choose $\text{Re} = 1$, $\text{Ca} = 1$, $\text{Pe} = 100$, and
 737 $\text{Cn} = h$. The microstructure surface is hydrophobic with respect to phase A with a
 738 contact angle $\vartheta = 135^\circ$. The buffer surface and outflow boundary are neutral, namely
 739 $\vartheta = 90^\circ$.

740 Figure 5 shows snapshots of the order parameter field as well as its values along
 741 the plane $\{(x, y, z) \in \Omega : z = 0.5\}$ in mountain views. Similar to the previous example,
 742 we employ a rainbow color scale that maps the values in $[-1, 1]$ from blue to red for
 743 plotting the order parameter field. The center of the diffusive interface is colored green.
 744 The values outside $[-1, 1]$ are marked in black. We observe that phase A invades
 745 the microstructure while staying away from the solid surfaces due to the wettability
 746 constraint. The top two rows correspond to the simulation without applying any
 747 limiter whereas the bottom two rows correspond to the simulation applying our two-
 748 stage limiting strategy. Our limiters remove overshoot and undershoot. The fluid
 749 dynamics are similar for both cases.

750 Figure 6 shows the number of iterations of the Douglas–Rachford algorithm on
 751 each time step as well as the asymptotic linear convergence rates of selected time
 752 steps. Here, the errors $\|\mathbf{y}^k - \mathbf{y}^*\|_2$ and $\|\mathbf{x}^k - \mathbf{x}^*\|_2$ are measured in a similar way as
 753 explained in the previous example. A numerical way of getting an exact value of r
 754 is to run the Douglas–Rachford iterations sufficiently many times with small enough
 755 tolerance and count the number of entries that stay out of the bounds in \mathbf{y}^* . Using
 756 the exact r to compute the principal angle θ_{N-r} , the numerical results match our
 analysis, see Figure 6.

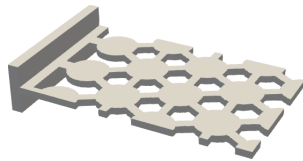


FIG. 4. *The computational domain of the microstructure simulation.*

757

758 **4.4. Merging droplets.** This example deals with droplets of fluid surrounded
 759 by another fluid. In a capillary-forces-dominated merging process, the large drop-
 760 let wobbles several times and eventually evolves into the most thermodynamically
 761 favorable configuration, e.g., a single spherical droplet.

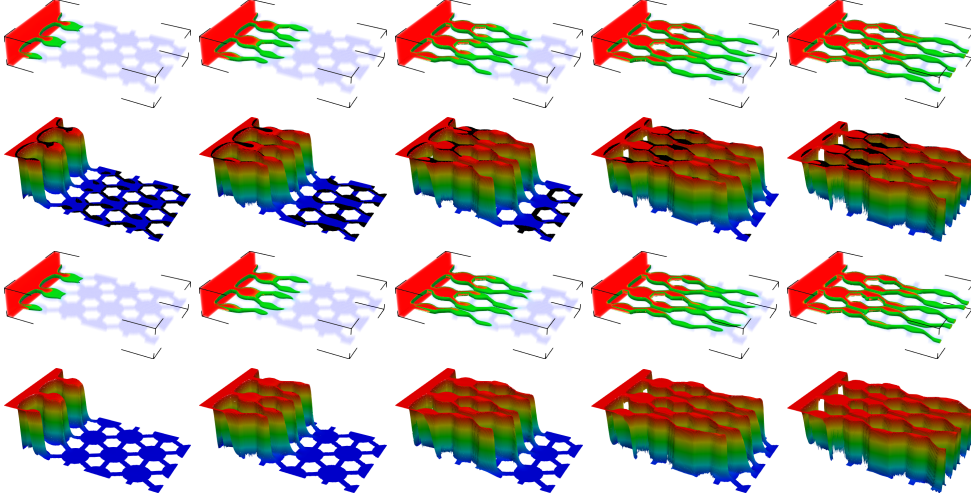


FIG. 5. Selected snapshots at time steps 50, 100, 150, 200, and 250. The first and third rows: 3D views of the evolution of the order parameter field. The second and fourth rows: plots of order parameter warped along the plane $\{z = 0.5\}$. The top two rows are without limiters and the bottom two rows are with our limiters.

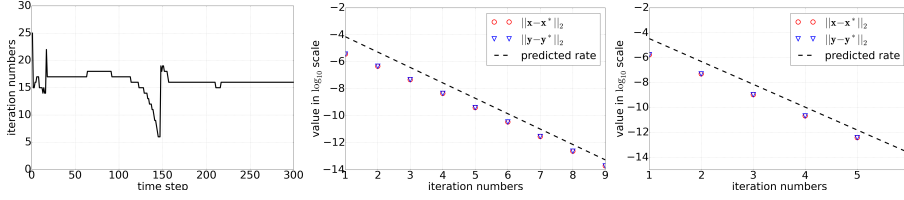


FIG. 6. The left top figure shows the number of Douglas–Rachford iterations at each time step. The middle and right figures show the asymptotic linear convergence at time steps 150 and 250, where the principal angle θ_{N-r} is computed by using exact values of r .

762 Let us consider four different scenarios. In the first scenario, we use constant
 763 mobility with GL polynomial potential and we do not apply any limiter. In the
 764 rest scenarios, we apply our two-stage limiting strategy. In the second scenario, we
 765 use constant mobility with GL polynomial potential. In the third scenario, we use
 766 constant mobility with FH logarithmic potential (parameters $\alpha = 0.3$ and $\beta = 1$). And
 767 in the fourth scenario, we use degenerate mobility with GL polynomial potential.

768 Let $\Omega = (0, 1)^3$ to be a closed system, $\partial\Omega = \partial\Omega^{\text{wall}}$ and set the initial velocity
 769 field $\mathbf{v}^0 = \mathbf{0}$. Four droplets of phase A are initially in a non-equilibrium configuration,
 770 surrounded by phase B, i.e., the initial order parameter field is prescribed by

$$771 \quad \phi^0 = \max \left\{ -1, \tanh \left(\frac{r_1 - \|x - \mathbf{a}_0\|}{\sqrt{2} C_n} \right), \tanh \left(\frac{r_1 - \|x - \mathbf{a}_1\|}{\sqrt{2} C_n} \right), \tanh \left(\frac{r_2 - \|x - \mathbf{a}_2\|}{\sqrt{2} C_n} \right), \tanh \left(\frac{r_2 - \|x - \mathbf{a}_3\|}{\sqrt{2} C_n} \right) \right\},$$

772 where $\mathbf{a}_0 = [0.35, 0.35, 0.35]^T$ and $\mathbf{a}_1 = [0.65, 0.65, 0.65]^T$ are the centers of the
 773 two initial larger droplets with radius $r_1 = 0.25$; and $\mathbf{a}_2 = [0.75, 0.25, 0.25]^T$ and
 774 $\mathbf{a}_3 = [0.25, 0.75, 0.75]^T$ are the centers of the two initial smaller droplets with radius
 775 $r_2 = 0.16$. For the FH logarithmic potential, we use $0.997\phi^0$ as the initial order
 776 parameter field to make its value away from the singularity. We uniformly partition
 777 domain Ω by cubic elements with the mesh resolution $h = 1/50$ and take the time

778 step size $\tau = 10^{-4}$. For physical parameters, we choose $\text{Re} = 1$, $\text{Ca} = 10^{-4}$, $\text{Pe} = 1$,
 779 $\text{Cn} = h$, and the contact angle $\vartheta = 90^\circ$ on $\partial\Omega$.

780 Figure 7 shows snapshots of the order parameter field. The center of the diffusive
 781 interface is colored green and the bulk phases are colored transparent. We see the
 782 merging of the four droplets, the intermediate wobbling stages, and the final equilib-
 783 rium configuration of a spherical droplet. We observe from Figure 7 that the fluid
 784 dynamics are visually similar in these scenarios. However, there are visible differences
 785 in certain one dimensional profiles, see Figure 8 for the order parameters at the line
 786 $\{(x, y, z) \in \Omega : x = y = z\}$.

787 Figure 8 shows values of order parameter along the diagonal $\{(x, y, z) \in \Omega : x =$
 788 $y = z\}$ of the computational domain. In scenario 1, we observe bulk shift at near
 789 steady state, which is as expected since no limiters are applied. In scenarios 2 and 4,
 790 our limiters remove overshoots and undershoots. In scenario 3, the FH logarithmic
 791 potential ensures bounds without bulk shift. The cell average limiter (1.7) is not
 792 triggered but the Zhang–Shu limiter is triggered. The global mass is conserved, see
 793 the left subfigure in Figure 9.

794 We plot the number of iterations of the Douglas–Rachford algorithm on each
 795 time step, see the right two subfigures in Figure 9. We check the asymptotic linear
 796 convergence rates and they match with our analysis. The errors $\|\mathbf{y}^k - \mathbf{y}^*\|_2$ and
 797 $\|\mathbf{x}^k - \mathbf{x}^*\|_2$ are measured in a similar way as in the previous example.

798 **5. Conclusion.** In this paper, we have analyzed the asymptotic linear conver-
 799 gence rate for using Douglas–Rachford splitting methods of a simple nonsmooth con-
 800 vex minimization, which forms a high order accurate cell average limiter. We obtain
 801 an explicit dependence of the convergence rate on the parameters, which gives a prin-
 802 ciple of parameter selection for accelerating the asymptotic convergence rate. Our
 803 optimization scheme is efficient and our two-stage limiting strategy is well-suited for
 804 high order accurate DG schemes for large-scale simulations.

805

REFERENCES

- 806 [1] R. BAILO, J. CARRILLO, S. KALLIADASIS, AND S. PEREZ, *Unconditional bound-preserving and*
 807 *energy-dissipating finite-volume schemes for the Cahn–Hilliard equation*, Communications
 808 *in Computational Physics*, (2023).
 809 [2] J. W. BARRETT, J. F. BLOWEY, AND H. GARCKE, *Finite element approximation of the Cahn–*
 810 *Hilliard equation with degenerate mobility*, SIAM Journal on Numerical Analysis, 37 (1999),
 811 pp. 286–318.
 812 [3] A. BECK, *First-Order Methods in Optimization*, SIAM, 2017.
 813 [4] A. CARLSON, M. DO-QUANG, AND G. AMBERG, *Dissipation in rapid dynamic wetting*, Journal
 814 *of Fluid Mechanics*, 682 (2011), pp. 213–240.
 815 [5] A. CHAMBOLLE AND T. POCK, *An introduction to continuous optimization for imaging*, Acta
 816 *Numerica*, 25 (2016), pp. 161–319.
 817 [6] W. CHEN, C. WANG, X. WANG, AND S. M. WISE, *Positivity-preserving, energy stable numerical*
 818 *schemes for the Cahn–Hilliard equation with logarithmic potential*, Journal of Computa-
 819 *tional Physics*: X, 3 (2019), p. 100031.
 820 [7] Q. CHENG AND J. SHEN, *A new Lagrange multiplier approach for constructing structure pre-*
 821 *serving schemes, I. Positivity preserving*, Computer Methods in Applied Mechanics and
 822 *Engineering*, 391 (2022), p. 114585.
 823 [8] Q. CHENG AND J. SHEN, *A new Lagrange multiplier approach for constructing structure pre-*
 824 *serving schemes, II. Bound preserving*, SIAM Journal on Numerical Analysis, 60 (2022),
 825 pp. 970–998.
 826 [9] L. DEMANET AND X. ZHANG, *Eventual linear convergence of the Douglas–Rachford iteration*
 827 *for basis pursuit*, Mathematics of Computation, 85 (2016), pp. 209–238.
 828 [10] Q. DU, L. JU, X. LI, AND Z. QIAO, *Maximum bound principles for a class of semilinear*
 829 *parabolic equations and exponential time-differencing schemes*, SIAM Review, 63 (2021),

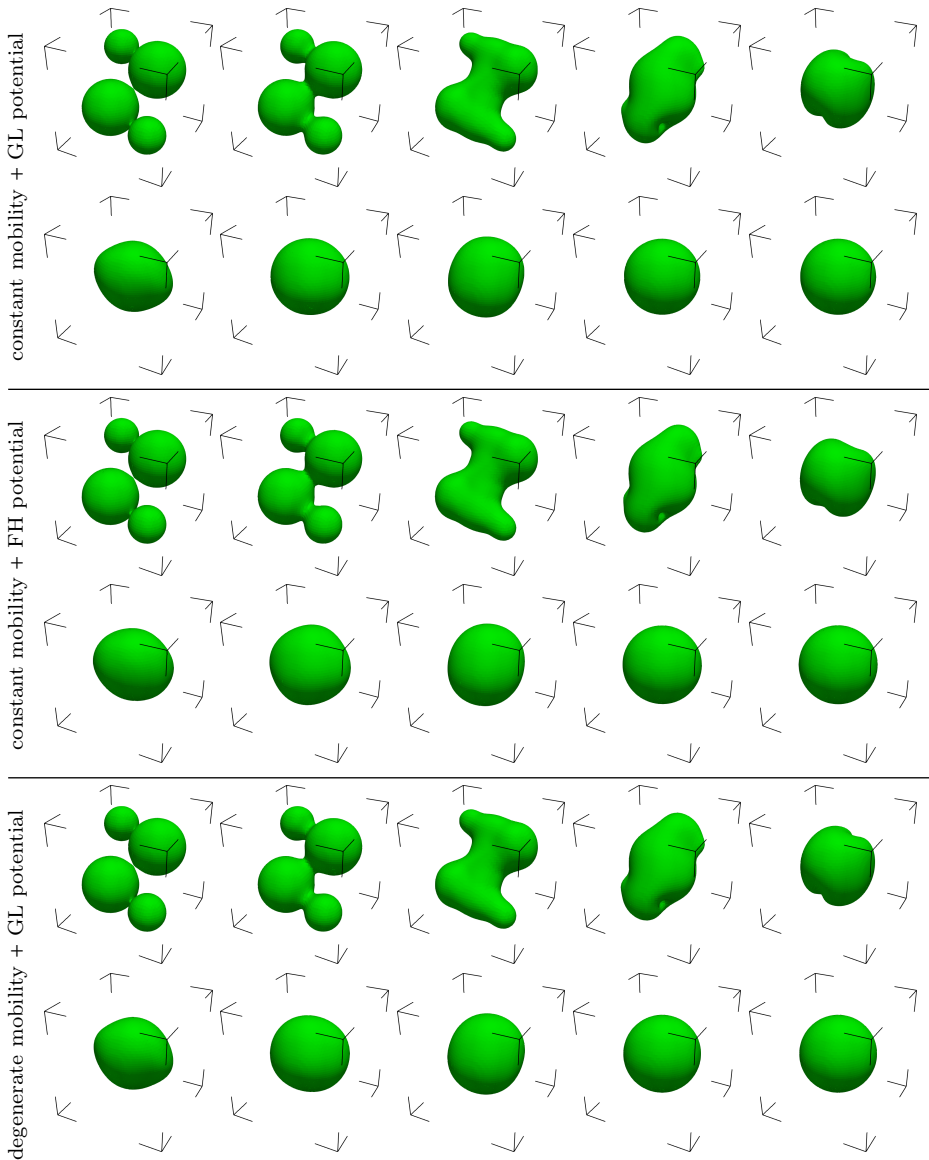


FIG. 7. 3D views of the evolution of the order parameter field. Selected snapshots at time steps 1, 3, 11, 23, 39, 56, 72, 90, 256, and 512. The dynamics are visually similar in these scenarios. However, there are visible differences in certain 2D profiles, see Figure 8.

- 830 pp. 317–359.
 831 [11] A. ERN AND J.-L. GUERMOND, *Invariant-Domain-Preserving High-Order Time Stepping:*
 832 *I. Explicit Runge–Kutta Schemes*, SIAM Journal on Scientific Computing, 44 (2022),
 833 pp. A3366–A3392.
 834 [12] C. FAN, X. ZHANG, AND J. QIU, *Positivity-preserving high order finite difference WENO*
 835 *schemes for compressible Navier-Stokes equations*, Journal of Computational Physics, 467
 836 (2022), p. 111446.
 837 [13] M. FORTIN AND R. GLOWINSKI, *Augmented Lagrangian Methods: Applications to the Numerical*
 838 *Solution of Boundary-value Problems*, Elsevier, 2000.
 839 [14] F. FRANK, C. LIU, F. ALPAK, AND B. RIVIERE, *A finite volume/discontinuous Galerkin method*
 840 *for the advective Cahn–Hilliard equation with degenerate mobility on porous domains stem-*

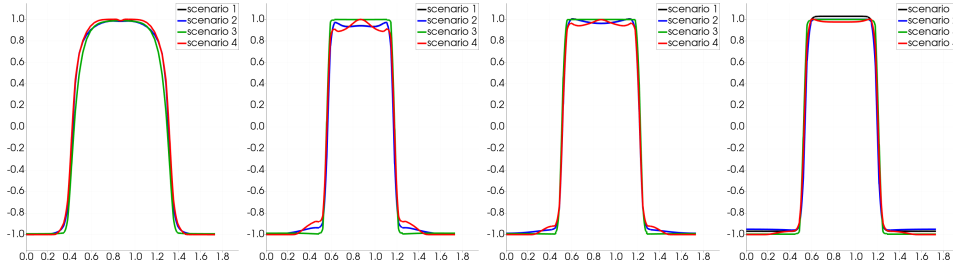


FIG. 8. Plots of order parameter extracted along the line $\{(x, y, z) \in \Omega : x = y = z\}$. Selected snapshots at time steps 23, 56, 90, and 512. Scenario 1: constant mobility with GL polynomial potential and do not apply any limiter. The rest scenarios apply limiters. Scenario 2: constant mobility with GL polynomial potential. Scenario 3: constant mobility with FH logarithmic potential. Scenario 4: degenerate mobility with GL polynomial potential.

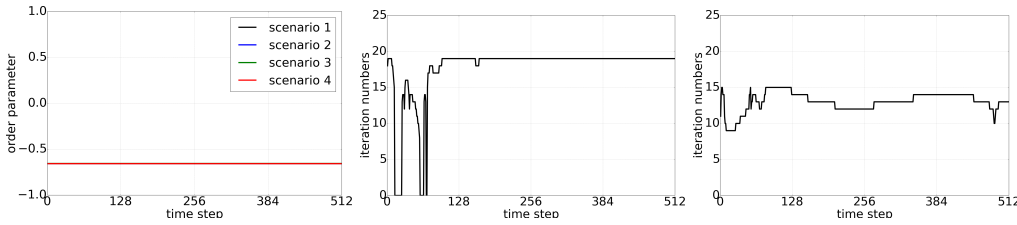


FIG. 9. Left: the average of order parameter at each time step. Middle and right: the number of Douglas–Rachford iterations for scenario 2 and 4 at each time step. Scenario 1: constant mobility with GL polynomial potential and do not apply any limiter. The rest scenarios apply limiters. Scenario 2: constant mobility with GL polynomial potential. Scenario 3: constant mobility with FH logarithmic potential. Scenario 4: degenerate mobility with GL polynomial potential.

841 *ming from micro-CT imaging*, Computational Geosciences, 22 (2018), pp. 543–563.
 842 [15] F. FRANK, C. LIU, F. O. ALPAK, S. BERG, AND B. RIVIERE, *Direct numerical simulation of flow*
 843 *on pore-scale images using the phase-field method*, SPE Journal, 23 (2018), pp. 1833–1850.
 844 [16] F. FRANK, C. LIU, A. SCANZIANI, F. O. ALPAK, AND B. RIVIERE, *An energy-based equilibrium*
 845 *contact angle boundary condition on jagged surfaces for phase-field methods*, Journal of
 846 *Colloid and Interface Science*, 523 (2018), pp. 282–291.
 847 [17] F. FRANK, A. RUPP, AND D. KUZMIN, *Bound-preserving flux limiting schemes for DG dis-*
 848 *cretizations of conservation laws with applications to the Cahn–Hilliard equation*, Com-
 849 *puter Methods in Applied Mechanics and Engineering*, 359 (2020), p. 112665.
 850 [18] V. GIRAULT, B. RIVIERE, AND M. WHEELER, *A discontinuous Galerkin method with nonover-*
 851 *lapping domain decomposition for the Stokes and Navier–Stokes problems*, Mathematics of
 852 *Computation*, 74 (2005), pp. 53–84.
 853 [19] R. GLOWINSKI, *Finite element methods for incompressible viscous flow*, Handbook of Numerical
 854 *Analysis*, 9 (2003), pp. 3–1176.
 855 [20] T. GOLDSTEIN AND S. OSHER, *The split Bregman method for L1-regularized problems*, SIAM
 856 *Journal on Imaging Sciences*, 2 (2009), pp. 323–343.
 857 [21] J.-L. GUERMOND, P. MINEV, AND J. SHEN, *An overview of projection methods for incom-*
 858 *pressible flows*, Computer Methods in Applied Mechanics and Engineering, 195 (2006),
 859 pp. 6011–6045.
 860 [22] J.-L. GUERMOND, B. POPOV, AND I. TOMAS, *Invariant domain preserving discretization-*
 861 *independent schemes and convex limiting for hyperbolic systems*, Computer Methods in
 862 *Applied Mechanics and Engineering*, 347 (2019), pp. 143–175.
 863 [23] F. HUANG, J. SHEN, AND K. WU, *Bound/positivity preserving and unconditionally stable*
 864 *schemes for a class of fourth order nonlinear equations*, Journal of Computational Physics,
 865 460 (2022), p. 111177.
 866 [24] A. V. KNYAZEV AND M. E. ARGENTATI, *Majorization for changes in angles between subspaces,*
 867 *Ritz values, and graph Laplacian spectra*, SIAM Journal on Matrix Analysis and Applica-
 868 *tions*, 29 (2007), pp. 15–32.

- 869 [25] D. KUZMIN, *Explicit and implicit FEM-FCT algorithms with flux linearization*, Journal of
870 Computational Physics, 228 (2009), pp. 2517–2534.
- 871 [26] P.-L. LIONS AND B. MERCIER, *Splitting algorithms for the sum of two nonlinear operators*,
872 SIAM Journal on Numerical Analysis, 16 (1979), pp. 964–979.
- 873 [27] C. LIU, F. FRANK, F. O. ALPAK, AND B. RIVIERE, *An interior penalty discontinuous Galerkin*
874 *approach for 3D incompressible Navier–Stokes equation for permeability estimation of por-*
875 *ous media*, Journal of Computational Physics, 396 (2019), pp. 669–686.
- 876 [28] C. LIU, F. FRANK, C. THIELE, F. O. ALPAK, S. BERG, W. CHAPMAN, AND B. RIVIERE, *An*
877 *efficient numerical algorithm for solving viscosity contrast Cahn–Hilliard–Navier–Stokes*
878 *system in porous media*, Journal of Computational Physics, 400 (2020), p. 108948.
- 879 [29] C. LIU, R. MASRI, AND B. RIVIERE, *Convergence of a decoupled splitting scheme for the Cahn–*
880 *Hilliard–Navier–Stokes system*, SIAM Journal on Numerical Analysis (to appear), (2023).
881 arXiv:2210.05625.
- 882 [30] C. LIU, D. RAY, C. THIELE, L. LIN, AND B. RIVIERE, *A pressure-correction and bound-*
883 *preserving discretization of the phase-field method for variable density two-phase flows*,
884 Journal of Computational Physics, 449 (2022), p. 110769.
- 885 [31] C. LIU AND X. ZHANG, *A positivity-preserving implicit-explicit scheme with high order poly-*
886 *nomial basis for compressible Navier–Stokes equations*, arXiv:2305.05769, (2023).
- 887 [32] R. MASRI, C. LIU, AND B. RIVIERE, *A discontinuous Galerkin pressure correction scheme for*
888 *the incompressible Navier–Stokes equations: Stability and convergence*, Mathematics of
889 Computation, 91 (2022), pp. 1625–1654.
- 890 [33] R. MASRI, C. LIU, AND B. RIVIERE, *Improved a priori error estimates for a discontinuous*
891 *Galerkin pressure correction scheme for the Navier–Stokes equations*, Numerical Methods
892 for Partial Differential Equations, 39 (2023), pp. 3108–3144.
- 893 [34] Y. NESTEROV, *Gradient methods for minimizing composite functions*, Mathematical Program-
894 ming, 140 (2013), pp. 125–161.
- 895 [35] T. QIN AND C.-W. SHU, *Implicit positivity-preserving high-order discontinuous Galerkin meth-*
896 *ods for conservation laws*, SIAM Journal on Scientific Computing, 40 (2018), pp. A81–
897 A107.
- 898 [36] B. RIVIERE, *Discontinuous Galerkin methods for solving elliptic and parabolic equations: theory*
899 *and implementation*, SIAM, 2008.
- 900 [37] J. SHEN, *Modeling and numerical approximation of two-phase incompressible flows by a phase-*
901 *field approach*, in Multiscale Modeling and Analysis for Materials Simulation, World Sci-
902 entific, 2012, pp. 147–195.
- 903 [38] J. SHEN AND X. YANG, *Decoupled, energy stable schemes for phase-field models of two-phase*
904 *incompressible flows*, SIAM Journal on Numerical Analysis, 53 (2015), pp. 279–296.
- 905 [39] S. SRINIVASAN, J. POGGIE, AND X. ZHANG, *A positivity-preserving high order discontinuous*
906 *Galerkin scheme for convection–diffusion equations*, Journal of Computational Physics,
907 366 (2018), pp. 120–143.
- 908 [40] Z. SUN, J. A. CARRILLO, AND C.-W. SHU, *A discontinuous Galerkin method for nonlinear par-*
909 *abolic equations and gradient flow problems with interaction potentials*, Journal of Com-
910 putational Physics, 352 (2018), pp. 76–104.
- 911 [41] G. TIERRA AND F. GUILLÉN-GONZÁLEZ, *Numerical methods for solving the Cahn–Hilliard equa-*
912 *tion and its applicability to related energy-based models*, Archives of Computational Meth-
913 ods in Engineering, 22 (2015), pp. 269–289.
- 914 [42] Z. XU, *Parametrized maximum principle preserving flux limiters for high order schemes solving*
915 *hyperbolic conservation laws: one-dimensional scalar problem*, Mathematics of Computa-
916 tion, 83 (2014), pp. 2213–2238.
- 917 [43] X. ZHANG, *On positivity-preserving high order discontinuous Galerkin schemes for compressible*
918 *Navier–Stokes equations*, Journal of Computational Physics, 328 (2017), pp. 301–343.
- 919 [44] X. ZHANG AND C.-W. SHU, *On maximum-principle-satisfying high order schemes for scalar*
920 *conservation laws*, Journal of Computational Physics, 229 (2010), pp. 3091–3120.
- 921 [45] X. ZHANG AND C.-W. SHU, *On positivity-preserving high order discontinuous Galerkin schemes*
922 *for compressible Euler equations on rectangular meshes*, Journal of Computational Physics,
923 229 (2010), pp. 8918–8934.